REMARKS

Information Disclosure Statement

The Examiner has requested detailed information regarding the FracCADE package referred to in the specification and drawings. Applicants have included herewith an excerpt from Reservoir Stimulation – Third Ed., Economides, M.J. and K.G. Nolte, Wiley and Sons, 2000. This excerpt describes approach used in the FracCADE package, particularly Section 6-3.2.

The Examiner has requested information pertaining to the "well known commercially available simulator" described in Mr. Siebrits affidavit. Attached is a copy of SPE 80935 which describes the GOPHER software system. This is the system referenced in the aforementioned affidavit.

The Examiner has requested information pertaining to the Lin and Keer three layer test. Applicants have included herewith an article from the Journal of Applied Mechanics (56 J. Appl. Mech.63-69) which describes this test.

The Examiner has made several objections to the specification. Applicants have submitted herewith substitute pages 4, 22 and 25 to address these objections. In addition, Applicants have amended equation (9).

Rejections Under 35 U.S.C. §112

The Examiner has rejected claims 1-4, 6-10 and 12-19 under 35 U.S.C. §112, first paragraph as containing subject matter which was not described in the specification in such a way as to enable one skilled in the art to make or use the invention.

Applicants respectfully traverse the rejection. Applicants have amended equation (9) to

indicate that amend the term "α_j" to "α_j^l" to indicate that it is layer dependent.

With regard to independent claim 6 and dependent claims 4, 7-10 and 12, the Examiner asserts that only partially active elements are updated. Applicants note that fully active elements include a global mass element and therefore do not require updating.

With regard to the rejection of claims 8 and 9, both claims have been amended to require that a time history of fluid volumes for pumping, fluid properties and logs are required in the first data set.

For these reasons, Applicants respectfully request that the Examiner withdraw this rejection of claims 1-4, 6-10 and 12-19.

Claims 3, 6-9 and 12 stand rejected under 35 U.S.C. §112, second paragraph as being indefinite for failing to particularly point out and distinctly claim the subject matter which Applicants regard as their invention. Applicants respectfully traverse the rejection.

Claim 3 has been amended to adapt the language suggested by the Examiner in paragraph 11 of the office action.

Claims 6-9 and 12 have been amended to correct the lack of antecedent basis for the limitation "the recalculation of fully active elements."

For these reasons, Applicants respectfully request that the Examiner withdraw this rejection of claims 3, 6-9 and 12.

Rejections Under 35 U.S.C. §103

Claims 1-3 and 13-19 stand rejected under 35 U.S.C. §103(a) as being unpatentable over GOPHER in view of Linkov, et al. Applicants respectfully traverse the rejection.
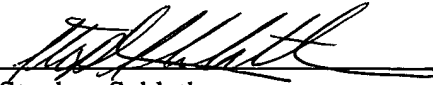

At the outset, Applicants note that Linkov was never coded into a simulator. Clearly, this is an important step in producing a system capable of modeling fractures. More importantly and as the Examiner may know, Linkov is not capable of modeling a formation where a hydraulic fracture touches or approaches an interface. This is a fundamental requirement for a hydraulic fracture simulator.

19

In addition and as the Examiner will note from the material supplied which details GOPHER, this simulator is based on equations which are incorrect for the present application.

In summary, for reasons detailed above, it is submitted that all claims now present in the application are allowable. Accordingly, allowance of all claims is submitted to be in order. Such action is respectfully requested.

The Commissioner is hereby authorized to charge or credit any fees to Deposit Account 04-1579(56.0468).

Respectfully submitted,

Stephen Schlather
Reg. No. 45,081

SCHLUMBERGER TECHNOLOGY CORPORATION
110 Schlumberger Drive, MD-1
Sugar Land, Texas 77478
281.285.4524
281.285.8569 (fax)

Geertsma and de Klerk also extended the model to include fluid leakoff, following Carter's (1957) method. Fluid loss is incorporated by assuming that it has no effect on fracture shape or pressure distribution. The volume of a two-wing KGD fracture is

$$V_f = \frac{\pi}{2} h_f L w_w. \qquad (6\text{-}33)$$

Performing a volume balance and solution procedure similar to that of Carter, they obtained

$$L = \frac{q_i w_w}{64 C_L^2 h_f} \left(e^{S^2} \text{erfc}(S) + \frac{2}{\sqrt{\pi}} S - 1 \right), \qquad (6\text{-}34)$$

where

$$S = \frac{8 C_L \sqrt{\pi t}}{\pi w_w}. \qquad (6\text{-}35)$$

To include the effects of spurt loss S_p, w_w should be replaced by $w_w + (8/\pi)S_p$, which is equivalent to the Carter relation with w replaced by $\bar{w} + 2S_p$ and $\bar{w} = \pi w/4$.

- Assumptions of the PKN and KGD models

Both the PKN and KGD models contain a number of assumptions that are revisited in this section. They assume that the fracture is planar (i.e., that it propagates in a particular direction, perpendicular to the minimum stress, as described in Chapter 3). They also assume that fluid flow is one-dimensional (1D) along the length of the fracture. In the case of the models described, they assume Newtonian fluids (although Perkins and Kern also provided solutions for power law fluids), and leakoff behavior is governed by a simple expression derived from filtration theory (Eq. 6-14). The rock in which the fracture propagates is assumed to be a continuous, homogeneous, isotropic linear elastic solid; the fracture is considered to be of fixed height or completely confined in a given layer; and one of two assumptions is made concerning the length to height ratio of the fracture—i.e., height is large (KGD) or small (PKN) relative to length. Finally, the KGD model includes the assumption that tip processes dominate fracture propagation, whereas the PKN model neglects fracture mechanics altogether.

Since these models were developed, numerous extensions have been made that relax these assumptions, the most important of which are the solutions for power law fluids. These two models

are still used to design treatments and are usually available as options in simulators.

Similar solutions can be derived for radial fractures (see Sidebar 6C).

6C. Radial fracture geometry models

Both Perkins and Kern (1961) and Geertsma and de Klerk (1969) considered radial fractures, which grow unconfined from a point source. This model is applicable when there are no barriers constraining height growth or when a horizontal fracture is created.

Geertsma and de Klerk formulated the radial model using the same arguments outlined in "Derivation of the Khristianovich–Geertsma–de Klerk model" (page 6-7). The fracture width is

$$w_w = 2.56 \left[\frac{\mu q_i R}{E'} \right]^{1/4} \qquad (6\text{C-}1)$$

and the radial length R is

$$R = \sqrt{\frac{q_i (4 w_w + 15 S_p)}{30 \pi^2 C_L^2} \left(e^{S^2} \text{erfc}(S) + \frac{2}{\sqrt{\pi}} S - 1 \right)} \qquad (6\text{C-}2)$$

where

$$S = \frac{15 C_L \sqrt{\pi t}}{4 w_w + 15 S_p}. \qquad (6\text{C-}3)$$

An explicit relationship for pressure can be derived by considering the solution for flow from a point source, in which case the pressure in the fracture is a function of the expression $\ln(r_w/R)$, where r_w is the radius of the wellbore. The no-fluid-loss approximations for the radial model are

$$w_w = 2.17 \left[\frac{\mu^2 q_i^3}{E'^2} \right]^{1/9} t^{1/9} \qquad (6\text{C-}4)$$

$$R = 0.52 \left[\frac{E' q_i^3}{\mu} \right]^{1/9} t^{4/9}. \qquad (6\text{C-}5)$$

The large-fluid-loss approximation for radial length is

$$R = \frac{1}{\pi} \left[\frac{q_i^2 t}{C_L^2} \right]^{1/4} \qquad (6\text{C-}6)$$

An expression for width in the case of large fluid loss was not provided but can be found from Eqs. 6C-1 and 6C-6.

6-3. Three-dimensional and pseudo-three-dimensional models

The simple models discussed in the previous sections are limited because they require the engineer to specify the fracture height or to assume that a radial fracture will develop. This is a significant limitation, because it is not always obvious from logs and other

data where or whether the fracture will be contained. Also, the fracture height usually varies from the well (where the pressure is highest) to the tip of the fracture. This limitation can be remedied by the use of planar 3D and pseudo-3D (P3D) models.

The three major types of hydraulic fracture models that include height growth are categorized according to their major assumptions.

- General 3D models make no assumptions about the orientation of the fracture. Factors such as the wellbore orientation or perforation pattern may cause the fracture to initiate in a particular direction before turning into a final preferred orientation (perpendicular to the far-field minimum in-situ stress). Simulators incorporating such models are computationally intensive and generally require a specialist to obtain and interpret the results. They are most applicable in research environments, for which they are used for studying details of fracture initiation and near-well complexities such as those discussed in Section 6-8, rather than overall fracture growth. One example of such a study was published by Brady *et al.* (1993). These models are not discussed further in this volume.

- Planar 3D models are based on the assumption that the fracture is planar and oriented perpendicular to the far-field minimum in-situ stress. No attempt is made to account for complexities that result in deviations from this planar behavior. Simulators based on such models are also computationally demanding, so they are generally not used for routine designs. They should be used where a significant portion of the fracture volume is outside the zone where the fracture initiates or where there is more vertical than horizontal fluid flow. Such cases typically arise when the stress in the layers around the pay zone is similar to or lower than that within the pay. This type of model is described in more detail in Section 6-3.1.

- P3D models attempt to capture the significant behavior of planar models without the computational complexity. The two main types are referred to here as "lumped" and cell-based. In the lumped (or elliptical) models, the vertical profile of the fracture is assumed to consist of two half-ellipses joined at the center, as shown in Fig. 6-4. The horizontal length and wellbore vertical tip extensions are calculated at each time step, and the assumed shape is matched to these positions. These models make the
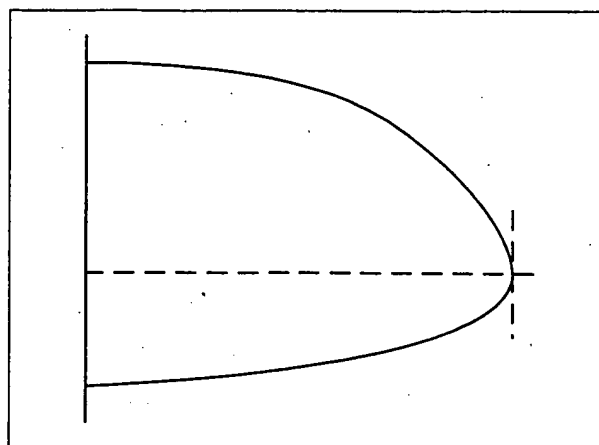

Figure 6-4. Conceptual representation of the lumped model.

inherent assumptions that fluid flow is along streamlines from the perforations to the edge of the ellipse and that the streamlines have a particular shape, derived from simple analytical solutions. Cell-based models treat the fracture as a series of connected cells. They do not prescribe a fracture shape, but generally assume plane strain (i.e., each cell acts independently) and do not fully couple the calculation of fluid flow in the vertical direction to the fracture geometry calculation.

In the fixed-height models described previously, no consideration is given to the layers surrounding the fractured zone. The planar and P3D models use data about the properties of the surrounding zones to predict the rate of growth into these zones. For the purpose of this chapter, planar 3D models are defined as those in which calculation of the full 2D fluid-flow field in the fracture is coupled to the 3D elastic response of the rock, and P3D models are defined as those that approximate either the coupling or the 3D elasticity in some manner.

Regardless of which type of model is used to calculate the fracture geometry, only limited data are available on typical treatments to validate the model used. For commercial treatments, the pressure history during treatment is usually the only data available to validate the model. Even in these cases, the quality of the data is questionable if the bottomhole pressure must be inferred from the surface pressure. The bottomhole pressure is also not sufficient to uniquely determine the fracture geometry in the absence of other information, such as that derived from tiltmeters and microseismic data (see Sidebar 6D). If a simulator incorporates the correct model, it should match both

6D. Field determination of fracture geometry

Fracture geometry can be determined by using the two techniques of microseismic activity and tiltmeters. Microseisms can be used to locate the fracture, thus providing estimates of its length and height, whereas tiltmeters can provide information about fracture width.

Microseisms

Although all models of hydraulic fracturing assume that the rock is a continuous medium, it is well known that reservoirs have natural fractures, bedding planes and other weakness features that respond as a noncontinuum. Such features have been used to image hydraulic fractures using seismic techniques.

Hydraulic fractures induce two large changes in the reservoir as they are created. The stress in the surrounding rocks is perturbed because of fracture opening, and the pore pressure is increased as a result of leakoff of the high-pressure fracturing fluid. Both of these features can result in the generation of large shear stresses on many of the weakness planes near the hydraulic fracture, resulting in small shear slippages called microseisms or microearthquakes.

Microseisms generate seismic waves that can be detected by sensitive seismic receivers in nearby wells. As shown in Fig. 6D-1, both compressional waves (P-waves) and shear waves (S-waves) can be generated by the microseism, and these two waves travel with different velocities. If a receiver can detect both the P- and S-waves, the time separation can be determined and the distance to the source inferred from

$$d = \frac{u_P u_S}{u_P - u_S}\left[t_s - t_p \right].\qquad(6D\text{-}1)$$

where u_P and u_S are the compressional and shear velocities, respectively, and t_s and t_p are the shear and compressional arrival times.

The direction in space can be determined by using a triaxial receiver to examine the amplitude of the P-wave. The P-wave has the characteristic that its particle motion (how the rock mass vibrates) is aligned with the direction of travel of the wave. By obtaining the orientation of the resultant amplitude vector at any time, the microseism can be traced back to its source.
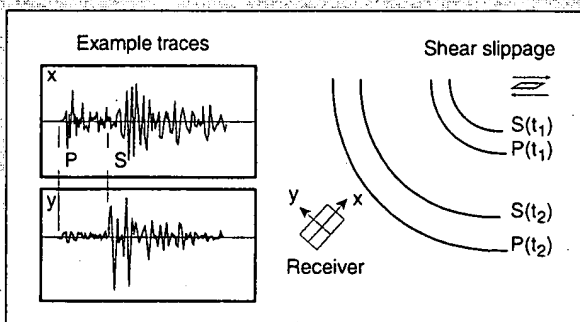
With multiple seismic receivers, triangulation techniques can be employed and greater accuracy obtained. With either approach, however, the objective is to locate the zone of microseisms surrounding the hydraulic fracture and deduce the size and shape of the fracture from this information.

Downhole tiltmeters

Width development in a hydraulic fracture results in elastic deformation of the formation. This deformation can be used for fracture diagnostics to provide significant information about fracture height and width and also about formation characteristics.

As a fracture is opened, the deformation of the rock extends for large distances into the reservoir. Although the deformation is small at distances of more than a few tens of feet, highly sensitive tiltmeter devices can measure these small changes in position. A tiltmeter does not actually measure the displacement of the earth, but rather the curvature of the displacement, and it is capable of measuring up to nanoradian resolution (a nanoradian is the angle induced by stretching a line from New York to Los Angeles and raising the New York side by the diameter of a pencil). Tiltmeters have long been used for surface diagnostics of earth movement, but the application of a string of downhole tiltmeters provides highly sensitive fracture data.

Figure 6D-2 shows a schematic of the tilt response of the formation measured in a well offset to the fracture treatment. The characteristic S-shaped curve is typical of tilt, as opposed to strain, and can be simply explained. Straight across from the fracture, the rock is pushed away, but is not tilted on the geometric axis of the fracture, and there is zero tilt. Above the fracture, the earth experiences curvature that is defined as negative for this example. The curvature reaches a maximum at a well-defined point and then decreases to zero as the distance from the fracture increases. The bottom is identical to the top, except that the curvature has the opposite direction and opposite sign.

Two aspects of this distribution are important for diagnostics. First, the locations of the maximum tilt values are a function of the height h_f of the fracture relative to the distance d away. Thus, fracture height can be quickly estimated. Second, the amplitude of the tilt is a function of the width of the fracture, so the width during fracturing, and possibly the final propped width, can be estimated as well.

Branagan et al. (1996) provided an example of the application of tiltmeters to the calculation of hydraulic fracture geometry.

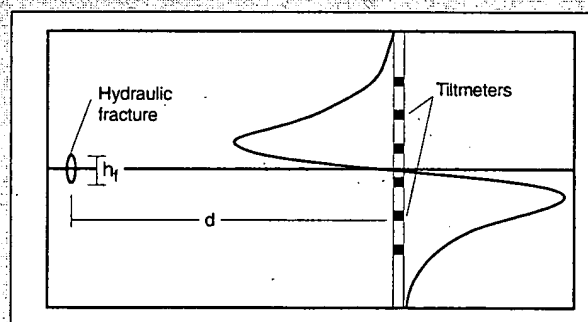Figure 6D-1. Microseismic traces at the receiver resulting from shear slippage.

Figure 6D-2. Tiltmeter response to hydraulic fracture width.

treating pressure and fracture geometry. These issues are addressed in Section 6-12 and Chapter 9.

6-3.1. Planar three-dimensional models

A planar fracture is a narrow channel of variable width through which fluid flows. The fracture geometry is defined by its width and the shape of its periphery (i.e., height at any distance from the well and length). Both the width at any point and the overall shape vary with time. They depend on the pressure distribution, which itself is determined by the pressure gradients caused by the fluid flow within the fracture. Because the relation between pressure gradient and flow rate is highly sensitive to the fracture width (Eq. 6-9), the geometry and fluid flow are tightly coupled. Although the mechanics of these processes are described separately in this section, the complexity of solving any fracture model lies in the close coupling between the different processes. Three separate problems are considered:

- width profile in a fracture of known shape and pressure distribution
- shape of the fracture
- flow of fluid in a fracture of known shape and width (i.e., known geometry).

Hirth and Lothe (1968) and Bui (1977) showed how the pressure and width in a fracture may be related. Basically, the width at any point (x,y) is determined by an integral of the net pressure over the entire fracture, expressed as

$$w(x,y) = \iint_S f(x-x', y-y')(p(x',y') - \sigma(x',y'))dx'dy',$$

(6-36)

where σ is the stress.

The details of the elastic influence function f in Eq. 6-36 are beyond the scope of this volume. Useable forms of Eq. 6-36 can be derived generally only for homogeneous linear elastic materials (see Sidebar 6E). In fracturing applications, the rock is usually also assumed to be isotropic.

The shape of the fracture evolves with time. In essence, the boundary (i.e., the vertical and horizontal tips) moves outward as the fluid provides sufficient energy to fracture the rock at the boundary. More complex tip behavior is discussed subsequently, but in this section it is assumed that this process is described by linear elastic fracture mechanics (LEFM). If the LEFM failure criterion is exceeded at any point on the fracture periphery, the fracture will extend until the criterion is again met. For simple shapes and pressure distributions, such as ellipses under constant pressure, the criterion can be specified analytically, similar to Eq. 6-3. For more complex shapes and pressure distributions, analytical solutions are not available. In these cases, it can be shown that a relatively simple criterion can be written in terms of the width near the tip and the critical stress intensity factor or fracture toughness K_{Ic}, which is introduced in Chapter 3:

$$w(x) = \frac{4\sqrt{2}K_{Ic}}{\sqrt{\pi}E'}\sqrt{x},$$

(6-37)

where x is the distance measured from the tip. Relations between fracture mechanics parameters such as the specific surface energy (used in Eq. 6-3) and the fracture toughness are provided in Chapter 3.

The fluid flow is described by equations for conservation of mass (a general form of Eq. 6-21, including the density ρ and expressed in terms of velocity u):

$$\left(\frac{\partial(\rho w u_x)}{\partial x} + \frac{\partial(\rho w u_y)}{\partial y}\right) + \frac{\partial}{\partial t}(\rho w) + 2\rho u_L = 0, \quad (6\text{-}38)$$

which can be written as a vector equation:

$$\nabla \cdot (\rho w \bar{u}) + \frac{\partial}{\partial t}(\rho w) + 2\rho u_L = 0,$$

(6-39)

and the conservation of momentum (a general form of Eq. 6-9) is

$$\rho\frac{D\bar{u}}{Dt} = -\nabla p - [\nabla \cdot \tau] + \rho\bar{g},$$

(6-40)

where τ is the shear stress and $\bar{g}$ is the acceleration of gravity.

The first two terms in Eq. 6-38 relate to the spatial change of the mass-flow vector, and the second two terms represent the storage resulting from width increases and leakoff, respectively. Equation 6-40 is a vector equation. The term on the left-hand side is the rate of change of momentum, and the terms on the right-hand side are the pressure, viscous and gravitational forces, respectively. It simply states that a small element of fluid accelerates because of the forces acting on it. This equation can be expanded and then simplified for the geometries of interest in hydraulic frac-

6E. Lateral coupling in pseudo-three-dimensional models

Assume that a fracture has a fixed height and that it consists of a number of elements each of constant width over the height (i.e., a KGD fracture). Let the grid points be represented by points x_i in the center of the elements with corners $(x_{l,i}, y_{b,i})$, $(x_{l,i}, y_{t,i})$, $(x_{r,i}, y_{t,i})$ and $(x_{r,i}, y_{b,i})$, as shown in Fig. 6E-1. Crouch and Starfield (1983) developed a boundary element solution technique called the displacement discontinuity method. They showed that the pressure at any point is given by

$$p(x_i) = \sum_k A_{ik} w_i$$ (6E-1)

where A_{ik} is an influence function of the form

$$A_{ik} = \frac{G}{4\pi(1-v)} I(x_{c,i}, y_{c,i}; x_{l,k}, x_{r,k}, y_{b,k}, y_{t,k}),$$ (6E-2)

where the influence function I is defined as

$$I = \frac{[(x_{c,i}-x_{r,k})^2 + (y_{c,i}-y_{t,k})^2]^{1/2}}{(x_{c,i}-x_{r,k})(y_{c,i}-y_{t,k})}$$
$$- \frac{[(x_{c,i}+x_{r,k})^2 + (y_{c,i}-y_{t,k})^2]^{1/2}}{(x_{c,i}+x_{r,k})(y_{c,i}-y_{t,k})}$$
$$+ \frac{[(x_{c,i}+x_{r,k})^2 + (y_{c,i}+y_{b,k})^2]^{1/2}}{(x_{c,i}+x_{r,k})(y_{c,i}+y_{b,k})}$$
$$- \frac{[(x_{c,i}-x_{r,k})^2 + (y_{c,i}+y_{b,k})^2]^{1/2}}{(x_{c,i}-x_{r,k})(y_{c,i}+y_{b,k})}$$ (6E-3)

To accurately solve Eq. 6E-1 requires a large number of elements. Also, it is difficult to extend directly to other shapes such as ellipses or for nonconstant heights. To overcome these problems, the equation is modified as follows. The width at any point can be written as

$$w(x_k) = w(x_i) + \Delta w_{ki}$$ (6E-4)

where Δw_{ki} is defined as
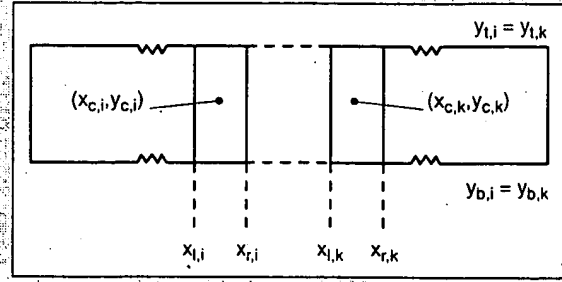
$$\Delta w_{ki} = w(x_k) - w(x_i).$$ (6E-5)

Figure 6E-1. Geometry for displacement continuity solution.

Equation 6E-1 can then be written as

$$p(x_i) = p(w_i) + p_{corr},$$ (6E-6)

where

$$p(w_i) = w(x_i) \sum_k A_{ik}$$ (6E-7)

$$p_{corr} = \sum_k A_{ik} \Delta w_{ki}.$$ (6E-8)

The term $w(x_i) \sum_k A_{ik}$ thus represents the pressure induced by a fracture of constant width $w(x_i)$. For a fracture of infinite length, this pressure would be exact if calculated using the plane strain solution. The term $p(w_i)$ can therefore be obtained as the sum of the plane strain solution and the effect of two semi-infinite fractures of $w - w_i$ attached at the tip of each fracture wing.

From Eq. 6E-2, the influence functions decrease with distance from an element. The advantages of the form of Eq. 6E-8 are that the corrections are smallest near the element where the widths are almost the same and that the self-correction is exactly zero by definition. The number of elements required to obtain an accurate solution is significantly reduced, and variable heights and other shapes are easily introduced. Lateral coupling is relatively easy to introduce to the explicit solution method because the pressure correction is simply added before the fluid velocities are calculated.

---

turing (see Sidebar 6F). For a particular component, such as the x component, Eq. 6-40 can be written as

$$\rho \frac{Du_x}{Dt} = -\frac{\partial p}{\partial x} - \left(\frac{\partial \tau_{xx}}{\partial x} + \frac{\partial \tau_{yx}}{\partial y} + \frac{\partial \tau_{zx}}{\partial z}\right) + \rho g_x.$$ (6-41)

A constitutive law relating the stresses τ to the flow rate is required to complete the description of fluid flow. In the case of steady flow in a narrow channel such as a fracture, the full details of the constitutive law are not required, because the narrow fracture width results in the complete dominance of some stress terms. The only terms of interest are the shear stresses induced by velocity gradients across the fracture. In addition, use is made of the lubrication approximation, so flow perpendicular to the fracture wall (the z direction) is neglected. With these assump-

tions, the equations for the stress in a Newtonian fluid reduce to

$$\tau_{xz} = \tau_{zx} = -\mu\left(\frac{\partial u_x}{\partial z}\right)$$
$$\tau_{yz} = \tau_{zy} = -\mu\left(\frac{\partial u_y}{\partial z}\right),$$ (6-42)

and Eq. 6-41 can be written as

$$\rho \frac{Du_x}{Dt} = -\frac{\partial p}{\partial x} + \mu\left(\frac{\partial^2 u_x}{\partial z^2}\right) + \rho g_x.$$ (6-43)

For the special case of a narrow channel (Poiseuille flow), where velocity gradients parallel to the flow are small and there is no flow perpendicular to the channel, the time-dependent term simplifies to a partial

6F. Momentum conservation equation for hydraulic fracturing

Equation 6-40 is a vector equation, for which a component can be written as

$$\rho \frac{Du_i}{Dt} = -\frac{\partial p}{\partial x_i} - \left(\frac{\partial \tau_{xi}}{\partial x} + \frac{\partial \tau_{yi}}{\partial y} + \frac{\partial \tau_{zi}}{\partial z} \right) + \rho g_i,$$ (6F-1)

where u is the velocity, g is the gravitational acceleration, and i is x, y or z. The term on the left side of Eq. 6F-1 is termed the substantial derivative, which is the rate of change seen by an observer moving with the fluid motion. It can be related to the usual partial derivative (i.e., the rate of change seen by a stationary observer) as

$$\frac{D}{Dt} = \frac{\partial}{\partial t} + u_x \frac{\partial}{\partial x} + u_y \frac{\partial}{\partial y} + u_z \frac{\partial}{\partial z}.$$ (6F-2)

Thus, Eq. 6F-2 can be expanded to

$$\rho \left(\frac{\partial u_i}{\partial t} + u_x \frac{\partial u_i}{\partial x} + u_y \frac{\partial u_i}{\partial y} + u_z \frac{\partial u_i}{\partial z} \right)$$
$$= -\frac{\partial p}{\partial x_i} - \left(\frac{\partial \tau_{xi}}{\partial x} + \frac{\partial \tau_{yi}}{\partial y} + \frac{\partial \tau_{zi}}{\partial z} \right) + \rho g_i.$$ (6F-3)

This completely general equation can be simplified for a narrow channel in an impermeable medium. Leakoff does not occur in this case, so components in the z direction can be neglected. In addition, the flow is assumed to be steady state, so time derivatives can be ignored. In this case, Eq. 6F-3 simplifies to

$$\rho \left(u_x \frac{\partial u_i}{\partial x} + u_y \frac{\partial u_i}{\partial y} \right)$$
$$= -\frac{\partial p}{\partial x_i} - \left(\frac{\partial \tau_{xi}}{\partial x} + \frac{\partial \tau_{yi}}{\partial y} + \frac{\partial \tau_{zi}}{\partial z} \right) + \rho g_i,$$ (6F-4)

for $i = 1$ or 2. Even for a permeable medium, Eq. 6F-4 is used. In this case, leakoff is treated as a sink term and included in the mass balance, but it is assumed not to affect the equations relating pressure, stress and fluid velocity.

Newtonian fluids

To make Eq. 6F-4 useful, the stress components must be determined, which is done by assuming a model of fluid behavior. For example, a Newtonian fluid is a model with one parameter, the viscosity μ. The stress components are

$$\tau_{xx} = \mu \frac{\partial u_x}{\partial x} + \frac{2}{3} \mu (\nabla \cdot u)$$

$$\tau_{yy} = 2\mu \frac{\partial u_y}{\partial y} + \frac{2}{3} \mu (\nabla \cdot u)$$

$$\tau_{zz} = 2\mu \frac{\partial u_z}{\partial z} + \frac{2}{3} \mu (\nabla \cdot u)$$

$$\tau_{xy} = \tau_{yx} = -\mu \left(\frac{\partial u_x}{\partial y} + \frac{\partial u_y}{\partial x} \right)$$

$$\tau_{yz} = \tau_{zy} = -\mu \left(\frac{\partial u_y}{\partial z} + \frac{\partial u_z}{\partial y} \right)$$

$$\tau_{zx} = \tau_{xz} = -\mu \left(\frac{\partial u_z}{\partial x} + \frac{\partial u_x}{\partial z} \right).$$ (6F-5)

The first three components of Eq. 6F-5 are the normal stresses, and the last three are the shear stresses. The last term of the normal components is zero for incompressible fluids. In the case of 1D flow between parallel plates, without leakoff, two of the velocity components are identically zero. In addition, conservation of mass implies that the third component cannot vary with position. Hence, all three normal components are identically zero. The equations thus reduce to those for shear flow. Although these assumptions are not strictly true in general, they are used for the flow calculations in hydraulic fracture modeling. It can also be shown that for a narrow channel, the velocity gradients perpendicular to the walls (the z direction) are much greater than those in the parallel directions. Finally, therefore, the stress components for a Newtonian fluid in a hydraulic fracture can be written as

$$\tau_{zx} = -\mu \left(\frac{\partial u_x}{\partial z} \right)$$

$$\tau_{zy} = -\mu \left(\frac{\partial u_y}{\partial z} \right).$$ (6F-6)

Substituting Eq. 6F-6 into Eq. 6F-4 obtains

$$\rho \left(u_x \frac{\partial u_x}{\partial x} + u_y \frac{\partial u_x}{\partial y} \right) = -\frac{\partial p}{\partial x} + \mu \frac{\partial^2 u_x}{\partial z^2}$$

$$\rho \left(u_x \frac{\partial u_y}{\partial x} + u_y \frac{\partial u_y}{\partial y} \right) = -\frac{\partial p}{\partial y} + \mu \frac{\partial^2 u_y}{\partial z^2} + \rho g.$$ (6F-7)

For 1D flow along the fracture length, as typically assumed in P3D models, Eq. 6F-7 can be simplified to

$$\frac{\partial^2 u_x}{\partial z^2} = \frac{1}{\mu} \frac{\partial p}{\partial x}.$$ (6F-8)

Assuming zero slip (i.e., zero velocity at the fracture wall), the solution to Eq. 6F-8 is

$$u_x = \frac{1}{2\mu} \frac{\partial p}{\partial x} \left(z^2 - (w/2)^2 \right).$$ (6F-9)

Integrating to obtain the average velocity across the channel,

$$\bar{u}_x = \frac{-w^2}{12\mu} \frac{\partial p}{\partial x}.$$ (6F-10)

The flow rate per unit height is obtained by multiplying the average velocity by the width w.

In the case of 2D flow, the left-hand sides of Eq. 6F-7 are zero if inertia may be neglected. In this case for the y direction, an equation can be formed similar to Eq. 6F-10, except that it includes a gravitational term.

derivative of velocity with respect to time. It is usually assumed that the flow is steady state, which finally obtains

$$\frac{\partial p}{\partial x} = \mu \left(\frac{\partial^2 u_x}{\partial z^2} \right) + \rho g_x \qquad (6\text{-}44)$$

and a similar equation for the y component.

Equations 6-36 through 6-44 summarize the planar 3D model for Newtonian fluids. Similar results can be obtained for non-Newtonian fluids (see Sidebar 6G). These equations are generally not amenable to analytic solutions, but require a numerical simulation. In addition, although it is relatively straightforward to write the conceptual equations, efficient and robust numerical solutions are difficult to obtain. The primary reasons for this difficulty are the extremely close coupling of the different parts of the solution (e.g., fluid flow and solid deformation), the nonlinear relation between width and pressure, and the complexity of a moving-boundary problem.

The first numerical implementation of a planar model was reported by Clifton and Abou-Sayed (1979). In essence, their approach was to define

a small fracture, initiated at the perforations, divide it into a number of equal elements (typically 16 squares) and then begin solution of the equations. As the boundary extends, the elements distort to fit the new shape. One difficulty with such a solution is that the elements can develop large aspect ratios and very small angles, as shown in Fig. 6-5. The numerical schemes typically used to solve the equations do not usually perform well with such shapes.

A different formulation was described by Barree (1983), and numerous field applications have been reported (e.g., Barree, 1991). It neatly avoids the problem of grid distortion by dividing the layered reservoir into a grid of equal-size rectangular elements, which are defined over the entire region that the fracture may cover. In this case, the grid does not move. Instead, as the failure criterion is exceeded, the elements ahead of the failed tip are opened to flow and become part of the fracture, as shown in Fig. 6-6. Two limitations of this approach are that

- the number of elements in the simulation increases as the simulation proceeds, so that the initial number may be small, resulting in inaccuracy

---

6G. Momentum balance and constitutive equation for non-Newtonian fluids

The definition of a Newtonian fluid is the one-parameter relation between stress and velocity (Eq. 6G-5). In tensor notation, this can be written as

$$\tau_{ij} = -\mu \Delta_{ij} \qquad (6\text{G-}1)$$

where Δ is the rate of deformation tensor, with components

$$\Delta_{ij} = \frac{\partial u_i}{\partial x_j} + \frac{\partial u_j}{\partial x_i} \qquad (6\text{G-}2)$$

The viscosity may be a function of pressure and temperature or other variables, including the history of the fluid, but not of Δ. For non-Newtonian fluids, an equation similar to Eq. 6G-1 may be written:

$$\tau_{ij} = -\mu_a \Delta_{ij} \qquad (6\text{G-}3)$$

where μ_a is a function of Δ. For flows of the type of interest in fracturing, it can be shown that μ_a may depend only on Δ through a relation of the form

$$\mu_a = \mu_a(I_2), \qquad (6\text{G-}4)$$

where I_2 is the second tensor invariant:

$$I_2 = \sum_i \sum_j \Delta_i \Delta_j. \qquad (6\text{G-}5)$$

For example, for a power law fluid, the function μ_a is

$$\mu_a = K \left| \sqrt{\frac{I_2}{2}} \right|^{n-1} \qquad (6\text{G-}6)$$

and for a Bingham plastic

$$\mu_a = \mu_0 + \frac{\tau_0}{\sqrt{\frac{I_2}{2}}} \qquad (6\text{G-}7)$$

The commonly used consistency index K' is dependent on the flow geometry and is related to a basic fluid property, the generalized consistency index K (Eq. 6G-6). For parallel plates (i.e., in a slot), which can represent a fracture, the relationship is

$$K' = K \left(\frac{2n+1}{3n} \right)^n. \qquad (6\text{G-}8)$$

For a pipe it is

$$K' = K \left(\frac{3n+1}{4n} \right)^n. \qquad (6\text{G-}9)$$

The maximum difference between the two expressions is less than 4% for all values of n. For 1D flow of a power law fluid between parallel plates, the average fluid velocity is given by

$$\bar{u}_x = \left(\frac{1}{K} \right)^{1/n} \left(\frac{\partial p}{\partial x} \right)^{1/n} \frac{n}{1+2n} \left(\frac{w}{2} \right)^{\frac{1+n}{n}} \qquad (6\text{G-}10)$$

For the special case of the power law exponent $n = 1$, this reverts to the equation for a Newtonian fluid, with K' replaced by the viscosity. Table 6G-1 summarizes useful information for the laminar flow of both Newtonian and power law fluids under different geometries. However, the expressions for pressure drop are not generally applicable for drag-reducing fluids such as those used in hydraulic fracturing.

Table 6G-1. Summarized expressions for laminar flow of Newtonian and power law fluids.

|	Fluid Type	Pipe	Parallel Plates	Ellipse (zero eccentricity)
Reynold's number (N_{Re})	Newtonian	$\dfrac{\rho u D}{\mu}$	$\dfrac{2\rho u w}{\mu}$	$\dfrac{\pi \rho u w}{2\mu}$
	Power law	$\dfrac{8^{1-n}\rho D^n u^{2-n}}{K'_p}$	$\dfrac{3^{1-n}2^{2-n}\rho u^{2-n}w^n}{K'_{pp}}$	$\dfrac{\pi^{2-n}\rho u^{2-n}w^n}{2^n K'_{el}}$
Hydraulic diameter (D_H) Friction factor $\left(f=\left(\dfrac{D_H}{4L}\Delta p\right)\Big/\left(\dfrac{1}{2}\rho u^2\right)\right)$		D $16/N_{Re}$	$2w$ $24/N_{Re}$	$\pi w/2$ $2\pi^2/N_{Re}$
Velocity distribution	Newtonian	$u_i=2u\left[1-\left(\dfrac{2r}{D}\right)^2\right]$	$u_x=\dfrac{3u}{2}\left[1-\left(\dfrac{2y}{w}\right)^2\right]$	$u_x=2u\left[1-\left(\dfrac{2y}{w}\right)^2-\left(\dfrac{2z}{h_f}\right)^2\right]$
	Power law	$u_r=\left(\dfrac{3n+1}{n+1}\right)u\left[1-\left(\dfrac{2r}{D}\right)^{\frac{n+1}{n}}\right]$	$u_x=\left(\dfrac{2n+1}{n+1}\right)u\left[1-\left(\dfrac{2y}{w}\right)^{\frac{n+1}{n}}\right]$	
Pressure drop ($\Delta p/L$ or dp/dx)	Newtonian	$\dfrac{128\mu q}{\pi D^4}$	$\dfrac{12\mu q}{h_f w^3}$	$\dfrac{64\mu q}{\pi h_f w^3}$
	Power law	$\dfrac{2^{5n+2}q^n K}{\pi^n D^{3n+1}}$	$\left(\dfrac{4n+2}{n}\right)^n\dfrac{2q^n K}{h_f^n w^{2n+1}}$	See Eq. 6-57
K'		$K'_p=K\left(\dfrac{3n+1}{4n}\right)^n$	$K'_{pp}=K\left(\dfrac{2n+1}{3n}\right)^n$	–
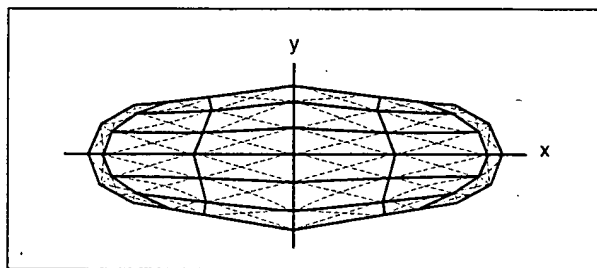
Figure 6-5. Planar 3D fracture divided into elements that were initially square.

Figure 6-6. Fixed-grid solution showing elements open to advance the fracture.

- the general size of the fracture must be estimated in advance of the simulation to ensure that a "reasonable" number of elements is used.

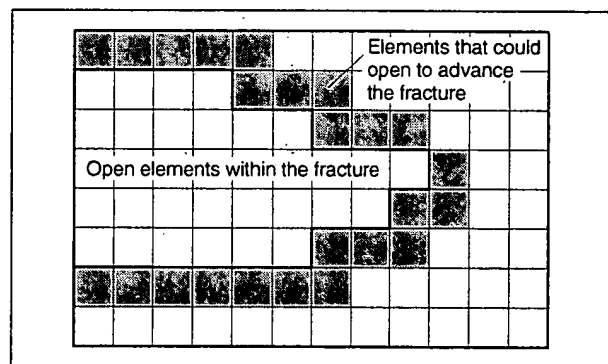In addition, this particular implementation has two simplifying assumptions, that a simplified method is used for representing modulus contrasts and a tensile strength criterion is used for fracture extension, rather than a fracture mechanics effect. The failure criterion is used to compare the stress at the center of all boundary elements with the material tensile strength.

If the strength is exceeded, then the element is assumed to open. However, the fracture-induced stress in the material near the tip of a fracture varies with the square root of the distance from the tip. Hence, the failure criterion is grid-resolution dependent.

6-3.2. Cell-based pseudo-three-dimensional models

In cell-based models, the fracture length is divided into a number of discrete cells. This is directly analogous to the planar models, except that only one direction is discrete instead of two. Fluid flow is assumed to be essentially horizontal along the length of the fracture, and the solid mechanics is typically simplified by assuming plane strain at any cross section. As in the PKN model, these assumptions make these models suitable primarily for reasonably contained fractures, which are long relative to their height.

These two assumptions allow separating the solid and fracture mechanics solution from the fluid flow as follows. Plane strain implies that each cross section acts independently of any other. In addition, the assumption of 1D fluid flow implies that the pressure in the cross section is always

$$p = p_{cp} + \rho g y, \qquad (6\text{-}45)$$

where p_{cp} is the pressure along a horizontal line through the center of the perforations and y is the vertical distance from the center of the perforations. Equation 6-45 is valid only if vertical fracture extension is sufficiently slow that the pressure gradient resulting from vertical flow can be neglected. This assumption that the vertical tips of the fracture are approximately stationary at all times is called the equilibrium-height assumption.

• Solid mechanics solution

With the equilibrium-height assumption, the solid mechanics solution simplifies to the determination of the fracture cross-sectional shape as a function of the net pressure, or p_{cp}. Simonson *et al.* (1978) derived this solution for a symmetric three-layer case. Fung *et al.* (1987) derived a more general solution for nonsymmetric multilayer cases. Following Fung *et al.* the stress intensity factors at the top and bottom tips K_{Iu} and K_{Il}, respectively, can be written in terms of the pressure at the center of the perforations p_{cp} and the closure stresses in the layers σ_i as

$$K_{Iu} = \sqrt{\frac{\pi h_f}{2}}\left[p_{cp} - \sigma_n + \rho_f g\left(h_{cp} - \frac{3}{4}h_f\right)\right]$$
$$+ \sqrt{\frac{2}{\pi h_f}}\sum_{i=1}^{n-1}(\sigma_{i+1} - \sigma_i)\left[\frac{h_f}{2}\cos^{-1}\left(\frac{h_f - 2h_i}{h_f}\right)\right.$$
$$\left. - \sqrt{h_f - (h_f - h_i)}\right]$$

$$(6\text{-}46)$$

$$K_{Il} = \sqrt{\frac{\pi h_f}{2}}\left[p_{cp} - \sigma_n + \rho_f g\left(h_{cp} - \frac{1}{4}h_f\right)\right]$$
$$+ \sqrt{\frac{2}{\pi h_f}}\sum_{i=1}^{n-1}(\sigma_{i+1} - \sigma_i)\left[\frac{h_f}{2}\cos^{-1}\left(\frac{h_f - 2h_i}{h_f}\right)\right.$$
$$\left. - \sqrt{h_f - (h_f - h_i)}\right],$$

$$(6\text{-}47)$$

where ρ_f is the fluid density, h_{cp} is the height at the center of the perforations, and h_i is the height from the bottom tip of the fracture to the top of the ith layer, as shown in Fig. 6-7.

This set of nonlinear equations can be solved by iteration. Assuming that the solution (two vertical tip positions plus the pressure) at one value of p_{cp} is known, a height increment is assumed. The incremental height growth in the two vertical directions is then calculated such that Eqs. 6-46 and 6-47 are both satisfied, and p_{cp} to obtain these positions is calculated. Finally, the width profile associated with this solution can be obtained as

$$w(y) = \frac{4}{E'}\left(p_{cp} + \rho_f g(h_{cp} - y) - \sigma_n\right)\sqrt{y(h_f - y)}$$
$$+ \frac{4}{\pi E'}\sum_{i=1}^{n-1}(\sigma_{i+1} - \sigma_i)$$
$$\left[(h_i - y)\cosh^{-1}\left(\frac{y}{|y - h_i|}\frac{h_f - 2h_i}{h_f} + \frac{h_i}{|y - h_i|}\right)\right.$$
$$\left. + \sqrt{y(h_f - y)}\cos^{-1}\left(\frac{h_f - 2h_i}{h_f}\right)\right], \qquad (6\text{-}48)$$

where y is the elevation measured from the bottom tip of the fracture.
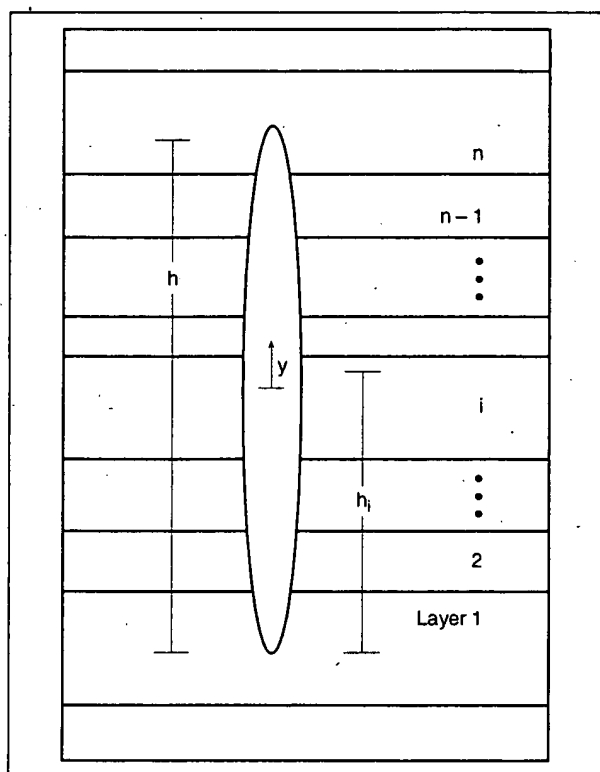
Figure 6-7. Definition of variables for the fracture containment problem.

Consider, for example, the symmetric three-layer case shown in Fig. 6-8. If the gravitational component is neglected, so that the problem is symmetric, then the penetrations into the two barriers are equal. In this case, Eq. 6-46 can be simplified significantly and written as (Simonson *et al.*, 1978)

$$K_{Iu} = K_{Il} = \sqrt{\frac{\pi h_f}{2}}\left[p_{cp} - \sigma_{pay} - \frac{2\Delta\sigma}{\pi}\cos^{-1}\left(\frac{h_{pay}}{h_f}\right)\right],$$

(6-49)

where $\Delta\sigma$ is the difference in stress between the central layer (pay zone) and the surrounding layers, and h_{pay} and σ_{pay} are the thickness and stress of the pay zone, respectively. Figure 6-9 shows fracture height as a function of net pressure, as calculated by Eq. 6-49.

Although Eq. 6-49 is for a special case, it shows two interesting practical results. First, penetration into the barrier layers occurs at a critical net pressure:

$$p_{net,crit} = \sqrt{\frac{2K_{Ic}^2}{\pi h_f}}.$$

(6-50)

For example, if K_{Ic} is 2000 psi/in.$^{1/2}$ and h_f is 20 ft [240 in.], the critical net pressure for breakthrough

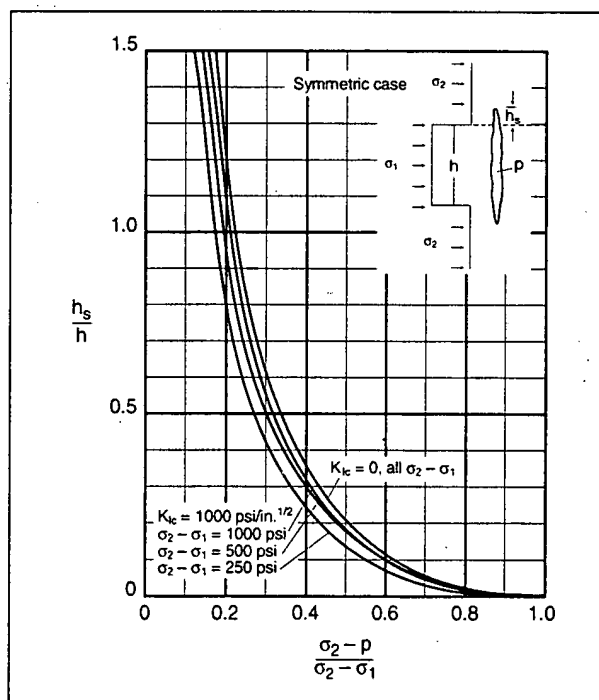**Figure 6-8.** Simple three-layer height growth problem.

Figure 6-9. Fracture height versus net pressure for symmetric barriers. h_s = penetration into the boundary layer.

is only about 100 psi. Second, the net pressure cannot reach the stress contrast because this would result in infinite fracture height.

In a typical cell-based simulator, a table of these solutions is calculated prior to simulating the fracture evolution rather than at each time step of the calculation, and the relations among width, pressure and height are used to greatly speed up the solution of the fluid flow equations (conservation of mass and momentum).

• Fluid mechanics solution

One of the major differences between planar 3D and P3D models is the fluid flow calculation. The fluid flow model in most P3D models is the same as that introduced by Nordgren (1972) (i.e., a 1D version of the model described for the planar 3D model). In this model, both vertical flow and the variation of horizontal velocity as a function of vertical position are neglected. This results in the inability of typical P3D models to represent several aspects of behavior, namely (Smith and Klein, 1995)

– effect of variations in width in the vertical direction on fluid velocity

– local dehydration, which is approximated as simultaneous dehydration over the entire height of the fracture

– fluid loss after tip screenouts (TSOs), when fluid flow through the proppant pack is ignored

– proppant settling resulting from convection or gravity currents.

The average velocity and width are used (width is replaced by cross-sectional area divided by height) to simplify the conservation of mass (Eq. 6-38 for an incompressible fluid) to

$$\frac{\partial A u}{\partial x} + \frac{\partial A}{\partial t} = -2 \sum_i \left(u_L h_L \right)_i, \qquad (6\text{-}51)$$

where u is the average cross-sectional velocity and u_L and h_L are the leakoff rate (Eq. 6-14) and height in each layer. Similarly, the conservation of momentum simplifies to

$$\frac{\partial p}{\partial x} = -\frac{\partial \tau_{xz}}{\partial z}. \qquad (6\text{-}52)$$

For a power law fluid with properties n and K,

$$\tau_{xz} = K \left(\frac{\partial u_x}{\partial z} \right)^n. \qquad (6\text{-}53)$$

Solving Eq. 6-52 with Eq. 6-53 with the no-slip boundary condition (i.e., zero velocity at the fracture wall), the average velocity across the channel is

$$\bar{u}_x = -\text{sgn}\left(\frac{\partial p}{\partial x} \right) \left(\left| \frac{\partial p}{\partial x} \right| \Big/ K \right)^{1/n} \frac{n}{1+2n} \left(\frac{w}{2} \right)^{\frac{1+n}{n}}, \qquad (6\text{-}54)$$

where sgn represents the sign of the quantity.

In the special case of a Newtonian fluid, $n = 1$ and $\mu = K$, and Eq. 6-54 becomes

$$\bar{u}_x = -\frac{w^2}{12\mu} \frac{\partial p}{\partial x}. \qquad (6\text{-}55)$$

To obtain the total flow rate across the height of the cross section, and hence an average velocity for substitution in Eq. 6-51, Eq. 6-54 is integrated from the bottom to the top tip of the cross section:

$$q = \int_{h_f} w(y) \bar{u}_x(y) dy. \qquad (6\text{-}56)$$

The average velocity is thus determined as

$$u = \frac{q}{A} = -\text{sgn}\left(\frac{\partial p}{\partial x} \right) \Phi \left[\left(\left| \frac{\partial p}{\partial x} \right| \Big/ 2K \right) \left(\frac{A}{h_f} \right)^{1+n} \right]^{1/n},$$

$$(6\text{-}57)$$

where the channel function Φ is

$$\Phi = \left(\frac{h_f}{A} \right)^{\frac{1+2n}{n}} \frac{n}{2+4n} \frac{1}{h_f} \int_{h_f} w(y)^{\frac{1+2n}{n}} dy. \qquad (6\text{-}58)$$

Relations for the PKN model with power law fluids can be derived following this approach (see Nolte, 1979, 1991).

– Laminar and turbulent flow

When fluid flows between parallel plates at a low rate without leakoff, any fluid element remains a fixed distance from the wall of the channel, except in a small entrance region. This is known as laminar flow. By contrast, in turbulent flow, eddies occur, and fluid is continually mixed. This mixing results in added friction and different flow behavior. The Reynold's number N_{Re} (defined in Table 6G-1) enables determining whether laminar or turbulent flow will occur. If N_{Re} exceeds 2100, flow will be turbulent. Inside the fracture, N_{Re} is typically well below this value, except for particularly thin fluids, such as acid.

- Rheology of fracturing fluids

Fracturing fluids are generally treated as power law fluids, and because they are shear thinning (i.e., viscosity decreases with increasing shear rate), n is usually less than 1. The effective parameters of the power law model K' and n' are typically derived from laboratory measurements (see Chapter 8) over a range of shear rates. For shear-thinning fluids, the apparent viscosity (derived from K' and n') decreases as shear rate increases, and the viscosity would be infinite at zero shear rate. In reality, limiting low- and high-shear viscosities occur and must be considered.

Fracturing fluid properties change with time and temperature. Typically, exposure to high temperatures reduces fluid viscosity. However, crosslinkers may cause initial viscosity increases prior to the degradation. The effects of temperature and time are included in numerical hydraulic fracture simulators, typically by means of tables of K' and n' versus time at a series of temperatures, which are similar to those in service company handbooks.

- Numerical solution of the model

The three basic solutions described for height-growth mechanics (pressure-width-height relation), conservation of mass and conservation of momentum (velocity-pressure relation) are coupled and solved simultaneously. There are several methods by which the coupled equations may be solved, two of which are introduced here. Either a fixed or moving mesh may be used for the two methods, as described previously for planar 3D models. In this section, the explicit finite-difference method is introduced with a grid that moves with the fluid and an implicit method is described. In each case, prior to starting the simulation of the fracture evolution, a table of the pressure-height-width relation (from the equilibrium-height solution) is calculated as described for "Solid mechanics solution" in Section 6.3-2.

For the explicit finite-difference method, the fluid in the fracture at any time is divided into n elements, each with a cross-sectional area A_i and bounded by two vertical surfaces at x_i and x_{i+1}, moving at velocities u_i and u_{i+1}, respectively, as shown in Fig. 6-10. (The grid is numbered such that $i = 1$ represents the tip to facilitate the addition
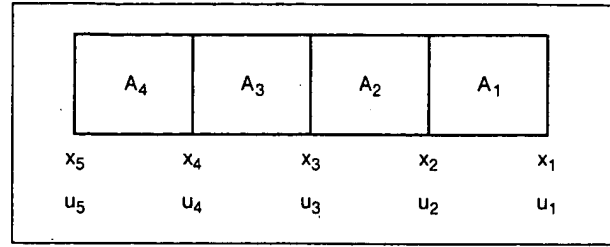

Figure 6-10. Fracture divided into elements with positions and velocities defined at grid points.

of new elements at the well, as necessary.) Mass-conservation Eq. 6-51 can be rewritten as

$$\frac{\partial A}{\partial t} = -2\sum_i (h_L u_L)_i - \frac{\partial Au}{\partial x}, \tag{6-59}$$

with the derivatives replaced by central finite-difference approximations to obtain

$$A_i^{t+\Delta t} = A_i^t - \frac{h}{\Delta x} V_L + A_i'\left(u_{i+1} - u_i\right)\frac{\Delta t}{\Delta x}, \tag{6-60}$$

where V_L represents the volume leaked off over the element of length Δx in time step Δt. The velocities are calculated at the grid points, and the area is assumed constant in each element. The cross-sectional area can thus be updated from the values of the velocities and areas at the previous time step. Once this has been done, the pressure at each cross section can be obtained from the solid mechanics solution by looking up the pressure in the precalculated pressure-height-width relation table for the corresponding area A. Pressure gradients can then be calculated using the approximation

$$\left.\frac{\partial p}{\partial x}\right|_i \approx \frac{p_{i-1} - p_i}{(x_{i-1} - x_{i+1})/2} \tag{6-61}$$

and new velocities obtained using Eq. 6-57. Once all the velocities are known at a given time, the positions of the grid points are updated using

$$x_i(t + \Delta t) = x_i(t) + u_i(t + \Delta t)\Delta t. \tag{6-62}$$

This method is known as a Lagrangian method because the grid coordinates move with the fluid. Leakoff causes each element to shrink and possibly even disappear as it penetrates farther into the fracture, limiting the usefulness of this method for modeling hydraulic fracturing treatments. In addition, new elements must continually be added at the wellbore. This makes it difficult to control how

many elements are present at any time or the sizes of the elements. Another approach is to introduce a fixed grid, as discussed for planar 3D models. This has the advantage that the number of elements in the simulation is relatively small near the beginning of the simulation when less accuracy is required and increases as the simulation progresses. Yet another approach is to introduce a moving mesh in which the grid points move at some reasonable velocity, for example, such that the fracture is always divided into a fixed number of equal-size elements (i.e., using a stretching coordinate system; see Sidebar 6H).

One of the primary limitations of explicit finite-difference methods, such as those introduced in the preceding text, is that the time step used in the calculation may not exceed a critical value to ensure stability. Because only quantities from the previous step are used in moving forward, numerical errors can grow larger from step to step if the time step is too large. In the development of a general hydraulic fracturing simulator using such differencing schemes, the time step must be chosen carefully to avoid stability problems and yet minimize the computation time. A simple stability analysis is in Sidebar 6H.

It has been found that in cases of high leakoff or large widths (such as TSO designs), the critical time step for stability may be too small for efficient solution of the system, limiting the utility of the

---

6H. Stretching coordinate system and stability analysis

Stretching coordinate system

One way to simplify grid point bookkeeping is to use a stretching coordinate system. If

$$X = \frac{x}{L(t)}, \tag{6H-1}$$

then X will always remain bounded between 0 and 1 while x varies between 0 and $L(t)$. Placing a grid on X will fully cover the fracture regardless of the growth characteristics. However, although the gridding is simplified, the complexity of the differential equation is increased. The derivatives are found as

$$\frac{\partial}{\partial x} = \frac{1}{L} \frac{\partial}{\partial X} \tag{6H-2}$$

$$\frac{\partial}{\partial t} = \frac{\partial}{\partial t} - \frac{X}{L} \frac{dL}{dt} \frac{\partial}{\partial X}. \tag{6H-3}$$

Equation 6-59 becomes

$$\frac{\partial A}{\partial t} - \frac{X}{L} \frac{dL}{dt} \frac{\partial A}{\partial X} = -\frac{1}{L} \frac{\partial q}{\partial X} - q_L, \tag{6H-4}$$

and the other equations of the system are similarly transformed.

Stability analysis

A full stability analysis for a nonlinear system is difficult, but an approximate time-step limitation can be found as follows. Assume that the pressure gradient can be written as

$$\frac{\partial p}{\partial x} = C_p \frac{\partial A}{\partial x}. \tag{6H-5}$$

In the case of the PKN model, where the fracture height h_f is fixed, $C_p = \beta h_f$, where β is defined by

$$p = \beta w. \tag{6H-6}$$

Substituting Eq. 6H-5 into Eq. 6-59 and applying the chain rule,

$$\frac{\partial A}{\partial t} = \frac{D}{n} A \left[A^{1+n} \frac{\partial A}{\partial x} \right]^{1/n-1} \left[A^{1+n} \frac{\partial^2 A}{\partial x^2} + (1+n) A^n \left(\frac{\partial A}{\partial x} \right)^2 \right], \tag{6H-7}$$

where absolute values must be assumed for all quantities, because an error analysis is being performed, and D is defined as

$$D = \frac{\Phi C_p^{1/n}}{\left(2 K h_f^{1+n}\right)^{1/n}}. \tag{6H-8}$$

The highest order term in Eq. 6H-7 is

$$\frac{D}{n} A \left[A^{1+n} \frac{\partial A}{\partial x} \right]^{1/n-1} \left[A^{1+n} \frac{\partial^2 A}{\partial x^2} \right]. \tag{6H-9}$$

If the derivative is expanded using a central difference approximation, the term in A_i becomes

$$\frac{-2D}{n(\Delta x)^2} \left| \frac{\partial A}{\partial x} \right|^{1/n-1} A^{3+1/n}. \tag{6H-10}$$

To investigate the effect of an error introduced into A, A is replaced by $A(1 + \varepsilon)$, which can be approximated (for small ε) as

$$\frac{-2D}{n(\Delta x)^2} \left| \frac{\partial A}{\partial x} \right|^{1/n-1} A^{3+1/n} \left(1 + \left(3 + \frac{1}{n} \right) \varepsilon \right). \tag{6H-11}$$

If a time step is taken (discretizing Eq. 6H-7 similar to Eq. 6-59), then the error ε grows to

$$E = \Delta t \frac{-2D}{n(\Delta x)^2} \left| \frac{\partial A}{\partial x} \right|^{1/n-1} A^{3+1/n} \left(1 + \left(3 + \frac{1}{n} \right) \varepsilon \right). \tag{6H-12}$$

For this error to reduce in magnitude, it must be smaller than $A\varepsilon$, which can occur only if

$$\Delta t < \frac{(\Delta x)^2}{2 A C_p C_v}, \tag{6H-13}$$

where the viscosity leakoff control coefficient C_v is

$$C_v = -\frac{(3n+1)v}{\frac{\partial p}{\partial x} n^2}. \tag{6H-14}$$

explicit scheme. An implicit finite-difference scheme, with no time-step limitation, may eliminate this limitation. In essence, implicit and explicit methods can be distinguished by the fact that explicit methods solve for quantities at one time step on the basis of only values at the previous time steps, whereas implicit methods include the use of quantities at the current time. This implies that a set of equations is set up and solved, because the quantities at the current time step must all be found simultaneously. For linear problems, a set of linear equations results, and these are easily solved by standard methods such as gaussian elimination. For the 1D flow problem, the implicit finite-difference formulation yields a tridiagonal system of equations (i.e., a sparse matrix with only three diagonals filled with nonzeros). Highly efficient solution techniques are available to solve such systems (e.g., Carnahan et al., 1969). For nonlinear problems, however, such methods can be complex and are not always much more efficient than explicit methods. Iteration is frequently required, because a nonlinear system is linearized. If the linearization approximation is inaccurate, it must be corrected and resolved.

Another method without the time-step limitation, and which avoids forming a system of equations, is a method using integrated or analytical elements. A similar method to that described in the following was the basis of the commercial time-sharing method made available by Amoco between 1981 and 1983 (Nolte, 1982, 1988a). Consider once again the basic equations of the PKN model with $x = \phi$ at the tip:

$$w = \frac{2p_{net}h_f}{E'} \qquad (6\text{-}63)$$

$$\frac{dp}{dx} = \frac{64q\mu}{\pi h_f w^3}. \qquad (6\text{-}64)$$

Substituting Eq. 6-64 for p into Eq. 6-63 obtains

$$\frac{E'}{2h_f}\frac{dw}{dx} = \frac{64q\mu}{\pi h_f w^3}. \qquad (6\text{-}65)$$

Detailed numerical simulations have shown that the velocity varies much more slowly than the flow rate q because the reduction in width toward the tip partially compensates for fluid leakoff and storage in the fracture. Instead of the Perkins and Kern

(1961) assumption that q is constant (Eq. 6-10), replacing q by $\pi u h_f w/4$ allows writing Eq. 6-65 as

$$\frac{dw}{dx} = \frac{32\mu h_f}{E'w^2}u \qquad (6\text{-}66)$$

or

$$w^2 dw = \frac{32\mu h_f}{E'}u\,dx. \qquad (6\text{-}67)$$

Integrating over a distance Δx obtains

$$w(x+\Delta x) = \left[w^3(x) + \int_x^{x+\Delta x}\frac{96\mu h_f}{E'}u\,dx\right]^{1/3}. \qquad (6\text{-}68)$$

If the terms under the integral can be assumed to be constant, this simplifies further to

$$w(x+\Delta x) = \left[w^3(x) + \frac{96\mu h_f}{E'}u\Delta x\right]^{1/3}. \qquad (6\text{-}69)$$

If the height is not constant and the fluid is non-Newtonian, a similar equation can be written for the cross-sectional area of the fracture by using the power law rheological parameters:

$$A'_{i+1} = \left[\left(A'_i\right)^{n+2} + \frac{(n+2)\pi K h_f^{n+3}}{E'\Phi^n}u^n\Delta x\right]^{1/(n+2)}, \qquad (6\text{-}70)$$

where

$$\Phi = \frac{n}{h_f(2+4n)}\int_{h_f}\left(\frac{w(y)}{\bar{w}}\right)^{\frac{1+2n}{n}}dy. \qquad (6\text{-}71)$$

For an analytical solution, Δx would be the entire fracture length (Nolte, 1991), and this would be combined with a tip criterion and a volume-balance equation. The numerical solution proceeds similarly, except that Δx is chosen sufficiently small to obtain an accurate solution. Fluid loss is integrated over the time step, which allows obtaining acceptable accuracy, even with large time steps. The solution method at each time step is as follows:

1. Estimate a tip velocity.

2. For each element, working in from the tip to the well,

   a. calculate an average fluid velocity based on the velocity at the outer side of the element and the estimated velocity at the inner side (At the first iteration, assume the inner fluid velocity is equal to the outer fluid velocity.)

b. determine the cross-sectional area at the inner
   side of the element for the estimated velocity
   by using Eq. 6-70

c. determine the velocity at the inner side such
   that the leakoff and element volume change
   during the time step result in a mass balance

d. repeat the iteration using the new velocity.

3. Compare the actual flow into the fracture with
   the wellbore velocity calculated by the iterative
   scheme in the preceding step.

4. Refine the estimate of the tip velocity using a
   Newton-Raphson method until volume balance
   is achieved, which typically takes two to four
   iterations.

This method of solving the equations is efficient
because the velocity does not vary significantly
along the fracture for typical cases. For typical
PKN cases with a single fluid, the fracture can
be divided into about 10 elements. For non-PKN
cases, the grid must be chosen sufficiently fine
that the integrand in Eq. 6-68 (which includes
effects of fluid rheology and fracture height) is
approximately constant in each element (because
the solution scheme is derived with the assump-
tion that it is constant).

Regardless of whether a moving- or fixed-grid
method is used, usually only a small number of
elements (about 10) is necessary to obtain a
reasonably accurate solution to the equations
described so far. However, other information may
be required at a much finer resolution. To achieve
this, the schedule is typically divided into a large
number of substages (about 100). Quantities such
as proppant concentration, fluid temperature and
acid concentration can then be tracked on this
finer grid. In addition, particularly in acid frac-
turing, it is desirable to track leakoff and etching
on a finer grid. To do this for methods using
a moving grid, a second grid that does not move
is established. Quantities such as reservoir tem-
perature, proppant bank height and leakoff vol-
ume in the reservoir are tracked on this solid-
based grid.

• Nonequilibrium-height solution

It was noted in "Solid mechanics solution" in
Section 6.3-2 that the assumption of slow height
growth allows creating a pressure-height-width
table prior to solving the equations of fracture evo-
lution. This so-called equilibrium-height assump-

tion is quite accurate, provided that the fluid is
moving relatively slowly in the vertical direction so
that the pressure drop resulting from vertical fluid
flow is negligible. This assumption is violated if
high-permeability zones are exposed, because fluid
must then move rapidly because of the increased
leakoff in such layers. Also, if the stress in the sur-
rounding zones is insufficient to confine the frac-
ture and the vertical tips extend quickly, then the
fluid must move quickly to fill the resulting frac-
ture. In either of these cases, the pressure gradient
resulting from vertical fluid flow may become
large, and the equilibrium-height assumption
becomes invalid at these locations in the fracture.

To remove this assumption and obtain valid
results from a simulator, some restriction must
be placed on height growth. For nonequilibrium-
height growth, the pressure gradient because of
fluid flow in the vertical direction must be approxi-
mated, based on the rate of height growth. It is
common to base this approximation on the KGD
model (e.g., Settari and Cleary, 1982). In Section
6-7 on tip effects, an analytical near-tip solution
developed by Lenoach (1994) is discussed that pro-
vides an expression for the net pressure of the form

$$p_{net} = E' \left(\frac{2\sqrt{2}(2+n)}{\pi(2-n)} \right)$$

$$\times \left[\frac{K'}{E'^n} \left(\frac{\cos[(1-\beta)\pi]}{\sin(\beta\pi)} \right) \right]^{1+n}$$

$$\left(\frac{2n+1}{n} \right)^n \frac{1}{n(2+n)^n} \right]^{1/(2+n)} u_{tip}^{n/(2+n)}, \quad (6\text{-}72)$$

where u_{tip} is the tip velocity and β is $2/(2 + n)$. As
previously noted, for a fracture under constant pres-
sure, the stress intensity factor is related to the net
pressure by

$$p_{net} = \frac{K_{Ic}}{\sqrt{\pi h_f / 2}}. \quad (6\text{-}73)$$

The Lenoach tip solution can be used to obtain
an apparent fracture toughness caused by the non-
zero tip velocity by combining Eqs. 6-72 and 6-73.
This effect can be added to the actual rock tough-
ness, and the sum is used in Eqs. 6-46 and 6-47
instead of the actual rock toughness to determine
the fracture height growth. The basic algorithm
used to move from one pair of vertical tip positions
to another during a time step is as follows:

1. Estimate the top and bottom tip velocities for the cell.

2. Calculate the new fracture tip positions at the end of the time step, using these velocities.

3. Calculate the stress intensity factors from Eqs. 6-46 and 6-47.

4. Determine the excess stress intensity factors (i.e., the calculated value minus the rock toughness).

5. Calculate the velocities required to generate these excess stress intensity factors, using Eqs. 6-72 and 6-73.

6. Compare the velocities with the guessed values and iterate until the correct velocities are found.

One of the advantages of the equilibrium-height models is the speed gained by precalculating a table of the fracture height-pressure relation. Not only is this not possible for the nonequilibrium model, but the iterative process to determine the tip positions can be time consuming. The nonequilibrium-height algorithm should therefore be used only when necessary because of the apparent rapid height growth indicated by the equilibrium-height calculation.

• Lateral coupling

In the description of the solid mechanics solution provided previously, the basic assumption is that individual cross sections act independently (i.e., plane strain in the horizontal direction, or laterally decoupled). This is implicit in the assumption that the pressure and width at any point are uniquely related. In reality, the pressure at any point is dependent not only on the local width, but also on the width distribution over the entire fracture, as discussed in Section 6-3.1 on planar 3D models. This lateral coupling is generally not important, unless the fracture wing length is less than the height. Even then, the fracture geometry will not be significantly different if lateral coupling is neglected, although the pressure response may be underestimated. Lateral coupling can be included in the solutions described previously (see Sidebar 6E).

The effect of lateral coupling during pumping is to increase the pressure at and near the well and to decrease it near the tip. Figure 6-11 shows the evolution of pressure during a treatment for a confined fracture simulated using the KGD, PKN and later-

ally coupled PKN models. The pressure predicted by the laterally coupled model is always higher than either the KGD or PKN solution would predict. It can also be shown that the width at the well is always smaller than that predicted by either of the simple models. The point in Fig. 6-11 where the pressure from the laterally coupled model is lowest (and where the pressures from the KGD and PKN models are equal) corresponds to a square, where the fracture wing length is one-half of the height. The pressure calculated by the laterally coupled model exceeds that predicted by the KGD or PKN model at this time by approximately 40%, which is comparable to the pressure in a radial fracture of similar dimensions.
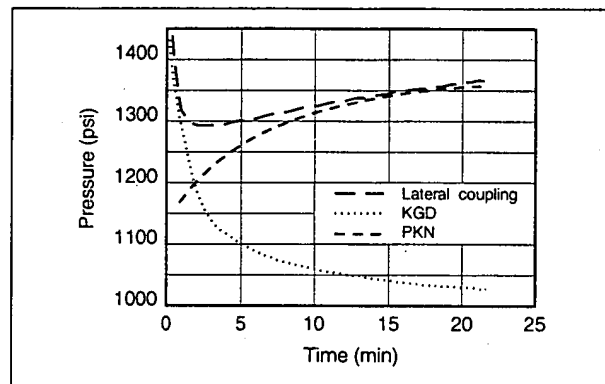

Figure 6-11. Pressure record with and without lateral coupling.

6-3.3. Lumped pseudo-three-dimensional models

Lumped models are an alternative to cell-based models and were first introduced by Cleary (1980b). Although more details are presented in subsequent paragraphs, it is worthwhile at this point to quote two sentences from the conclusions of his paper: "the heart of the formulae can be extracted very simply by a nondimensionalization of the governing equations; the remainder just involves a good physico-mathematical choice of the undetermined coefficients" and "results could be presented in the usual format of design charts, based on dimensionless groups extracted, . . . [a] more appealing procedure may be to program the solutions for a suitable pocket calculator, with the separately determinable γ or Γ coefficients and job parameters as input." Although numerous papers have

been presented on the use of this model (e.g., Cleary *et al.*, 1994), which is now on laptop computers rather than pocket calculators, these sentences capture the essence of lumped models in that they are extremely simple models and the key to their successful use is the selection of appropriate coefficients for the problem analyzed.

Like all the models presented previously, the starting point of the lumped model is the set of basic equations defining the hydraulic fracturing process, which are mass conservation (Eq. 6-39), the relation between the distribution of crack opening over the length of the fracture 2L, net pressure distribution (similar to Eq. 6-36) expressed as

$$p_{net}(x) = \int_{-L}^{L} I(x, x') w(x') dx', \qquad (6\text{-}74)$$

and conservation of momentum (Eq. 6-40) expressed as

$$\tilde{q} q^{m-1} = -\gamma_4 w^{2n-m+1} \tilde{\nabla} p / \mu, \qquad (6\text{-}75)$$

where γ_4 is the channel factor ($\frac{1}{12}$ for a Newtonian fluid), and various combinations of the power law factors m for turbulence and n enable consideration of both non-Newtonian fluids and turbulent flow.

In the lumped models, these equations are simplified by assuming a fracture shape and adopting a spatial averaging approach to reduce them to ordinary differential equations in time. This approach implicitly requires the assumption of a self-similar fracture shape (i.e., one that is the same as time evolves, except for a length scale). The shape is generally assumed to consist of two half-ellipses of equal lateral extent, but with different vertical extent.

It is instructive to consider some of the lumped equations for the KGD model (Cleary, 1980b). The mass balance is obtained by averaging over the fracture length:

$$\rho(q\overline{w} - Lq_L) = d(\gamma_3 \rho \overline{w} L)/dt, \qquad (6\text{-}76)$$

where

$$\overline{w} \approx (\gamma_1 p_{net}/E)L \qquad (6\text{-}77)$$

$$q^m \overline{w}^m \approx \gamma_5^m (\overline{w})^{2n+2}/L^2, \qquad (6\text{-}78)$$

where

$$\gamma_5^m \equiv \gamma_2 \gamma_4 E/(\gamma_1 \mu), \qquad (6\text{-}79)$$

which is the 1D form of Eq. 6-75. Equation 6-76 is similar to Eq. 6-15 (based on Carter, 1957) with the

addition of γ_3, and Eq. 6-77 is identical to that of Geertsma and de Klerk (1969) with γ_3 replacing $4(1 - v^2)$. Superficially, these equations are extremely simple, but the values of the γ coefficients are not always obvious and may not be constant. As noted by Crockett *et al.* (1989), these models are extremely general, with the degree of accuracy limited ultimately only by the effort invested in determination of the γ coefficients by detailed simulations, laboratory experiments or field studies.

For more general fracture shapes (i.e., with height growth), it is typically assumed that height growth is governed by a KGD-type solution and length growth by a PKN-type solution (Cleary *et al.*, 1983), although this is not a theoretical limitation of lumped models.

One area in which lumped models have been exploited extensively is in the development of computer software systems to apply and use pressure data during a treatment. Some of the key characteristics and requirements for such a software system are that (Crockett *et al.*, 1989)

- the physics is realistic and general
- execution time is much faster than treatment time to allow repetitive execution for pressure history matching
- the software can use improved estimates of parameters obtained in real time (i.e., during the treatment).

Although these real-time software systems are generally referred to as real-time hydraulic fracture models (e.g., Crockett *et al.*, 1989), the model itself is only a small part of the software and should address the first requirement listed (i.e., realistic and general physics). The second and third requirements are computer hardware and software design constraints. Because lumped models were developed for pocket calculators in 1980, they impose a minimal impact on computer hardware and systems. As computing power continues to improve, it will become possible to run increasingly sophisticated models during treatment execution either at the wellsite or remotely. There are other software design issues, such as robust execution with a wide variety of parameter values, easy import and superposition of actual data on model output, and graphical display, that are required for a useful software system for real-time applications. Discussion of these issues is beyond the scope of this volume.

W. Lin

L. M. Keer
Fellow ASME

Department of Civil Engineering,
Northwestern University,
Evanston, IL 60208

Analysis of a Vertical Crack in a Multilayered Medium

A general mathematical formulation to analyze cracks in a multilayered medium is constructed. First, a matrix for a single layer is formed in the Hankel transformed domain. Then a global matrix is formed by assembling together each layer matrix. The displacement and stress fields are obtained by inverting the Hankel transform. Finally, the planar crack problem is solved by the boundary integral method. The results given are the crack opening displacement and the stress intensity factors.

1 Introduction

Hydraulically-induced fracture is a technique being developed in the petroleum industry. The basic idea in the hydraulic fracture process is to use a highly pressurized fluid to break the rock so that the resources, oil or natural gas, can be more easily extracted. One of the difficult analytical problems for such fracturing processes is how to calculate the important quantities of physical interest when the process zone extends from the pay zone into upper and lower barriers. The methodology applied in this article, which studies one layer having upper and lower half space barriers, can also be applied to more general multilayered structures.

Multilayered structures are often encountered in many science and engineering branches such as geophysics, laminated composite materials, and highway pavements. The first systematic approach to multilayered media may be traced back to the Thompson (1950)–Haskell (1953) methods. Later, Gilbert and Backus (1966) introduced the propagator matrix method; Fuchs (1968, 1971) introduced the reflectivity method, and Pao and Gajewski (1977) have written a long article about generalized ray method.

The Green's functions in a multilayered media were derived by Luco and Apsel (1983). Xu and Mal (1987) give a simpler formulation and show that the problem can be solved by a personal computer. Kundu and Mal (1985) discussed the difficulty associated with the numerical integration in the transformed domain. Small and Booker (1986) solved a multilayered system by the flexibility matrix method. In Section 2, a general scheme to analyze the multilayered system is developed.

For the three-dimensional crack analysis in an unbounded medium, the boundary integral method is still preferred since the unknowns and equations occur only on the crack surfaces. The unknowns in the boundary integral method can be the crack opening displacement, Murakami and Nemat-Nasser

(1983), the first derivatives of crack opening displacement, Weaver (1977), or the second derivatives of the crack opening displacement. The choice depends on whether or not it is more convenient to avoid the high order singularity. Recent articles by Lee and Keer (1986) and Lin and Keer (1987) use the triangular element in the same manner as Murakami and Nemat-Nasser. Although the triangular element is somewhat easier for mesh generation, a four node element which may be generated via conformal mapping, can evaluate the finite part integral more easier. Other articles such as Krenk and Schmidt (1982), Martin and Wickmen (1983), Lin and Keer (1986), etc., are concerned with the scattering due to a crack in the frequency domain.

An extra difficulty encountered for analyzing a vertical crack in the multilayered medium is the point singularity that occurs at the intersection of the crack edge and the interface. Several articles, Benthem (1977), Bazant and Estenssoro (1979), and Somaratna and Ting (1986), have discussed this type of point singularity.

In Section 3, the boundary integral equation will be constructed by a Green's function approach. Triangular elements and a square root singularity along the crack edge will be adopted. Although the point singularity at interfaces is not considered in this article due to complexity, the interfacial phenomenon is discussed in the numerical results.

2 Mathematical Formulation for Multilayered Medium

To analyze a multilayered medium systematically, there are three basic principles involved. First, the matrix for a single layer is formed in such a way that the same formula can be applied to every layer. Next, the interfacial continuity conditions are executed in the transformed domain instead of in the spatial domain, since the mathematical operation required in the transformed domain is algebraic. The complexity of executing continuity conditions in the spatial domain can be found in Chan et al. (1974). Finally, to reduce the computational work, the solution is obtained by inverting the Hankel transform instead of inverting the double Fourier transform. Using these principles, the methodology to analyze the multilayered medium is constructed. Essentially, three types of matrices can be formed, namely the flexibility matrix, stiffness matrix, and propagator matrix. However, only the flex-

ibility matrix is considered in detail. The other two methods are described in Appendix A.

First, consider a linear elastic isotropic layer which occupies the spatial domain $0 \leq z \leq H$. Although initially there is no body force, such forces will be introduced later into the system. The displacement field in this case may be expressed in terms of Papkovich-Neuber potentials in rectangular coordinates. However, these potentials lead, unavoidably, to a double Fourier transform; therefore, the following alternative forms in cylindrical coordinates, Green and Zerna (1954), are considered:

$$u_z = \phi_{z,z} + z\phi_{r,z} - \kappa\phi_r \qquad (1a)$$

$$u_r = \phi_{z,r} + z\phi_{r,r} + 2\phi_{\theta,\theta}/r \qquad (1b)$$

$$u_\theta = \phi_{z,\theta}/r + z\phi_{r,\theta}/r - 2\phi_{\theta,r}. \qquad (1c)$$

Here $\kappa = 3 - 4\nu$, ν is Poisson's ratio, ϕ_z, ϕ_r, and ϕ_θ satisfy Laplace equations, and the comma denotes differentiation. These forms are particularly useful when the applied body force is a vertical or a horizontal point force since only the constant term or the first term in Fourier series expansion is needed. Next, the axially symmetric and asymmetric cases are considered.

(A) Axially Symmetric Case. In the axially symmetrical case, $u_\theta = \phi_\theta = 0$ and ϕ_z and ϕ_r have no angular dependence. Thus, the potentials can be solved by using the zeroth order Hankel transform. The results are exponential functions with unknown coefficients in the transformed domain. The displacement field is obtained by replacing the potentials in equation (1) with the Hankel integrals, and the stress field is obtained by further application of Hooke's law. Explicitly, the results are:

$$(u_z, \sigma_{zz}) = \int_0^\infty (U_{zz}, S_{zz})\xi J_0(\xi r)d\xi \qquad (2a)$$

$$(u_r, \sigma_{rz}) = \int_0^\infty (U_r, S_{rz})\xi J_1(\xi r)d\xi \qquad (2b)$$

and

$$\begin{Bmatrix} U_{zz} \\ U_r \\ S_{zz}/2\mu\xi \\ S_{rz}/2\mu\xi \end{Bmatrix} = (1/\alpha) \begin{bmatrix} -1 & -2\alpha-\xi z & -1 & 2\alpha-\xi z \\ -1 & 1-\xi z & 1 & 1+\xi z \\ 1 & \alpha+\xi z & -1 & \alpha-\xi z \\ 1 & -1+\alpha+\xi z & 1 & 1-\alpha+\xi z \end{bmatrix}$$

$$\times \begin{Bmatrix} A_1\exp(-\xi z) \\ A_2\exp(-\xi z) \\ A_3\exp[\xi(z-H)] \\ A_4\exp[\xi(z-H)] \end{Bmatrix} \qquad (3)$$

Here, μ is the shear modulus, $\alpha = 1 - 2\nu$, and $A_i(\xi)$ are functions to be determined from the boundary conditions. It should be noted that symbol U_{zz}, instead of U_z, is used in equation (2a); U_z will be reserved for the more lengthy asymmetric case.

To form the flexibility matrix, three vectors are defined as:

$$\{u\}^T = \{-U_{zz}(H), -U_r(H), U_{zz}(0), U_r(0)\} \qquad (4a)$$

$$\{\sigma\}^T = \{S_{zz}(H), S_{rz}(H), S_{zz}(0), S_{rz}(0)\} \qquad (4b)$$

$$\{A\}^T = \{A_1, A_2, A_3, A_4\}. \qquad (4c)$$

To form the stiffness matrix or propagator matrix, $\{u\}$ and $\{\sigma\}$ are defined in other forms. Details about the two other matrix methods are given in Appendix A. After defining $\{u\}$, $\{\sigma\}$, and $\{A\}$, the $\{u\} - \{A\}$ and $\{\sigma\} - \{A\}$ relationships are constructed by substituting $z = 0$ and $z = H$ into equation (3) in the form of equations (4a)-(4b). The results are written as:

$$\{u\} = [f_1]\{A\} \qquad (5a)$$

$$\{\sigma\} = [f_2]\{A\}. \qquad (5b)$$

The flexibility matrix for the layer is:

$$[f_v] = [f_1][f_2]^{-1} \qquad (6a)$$

$$[f_v]\{\sigma\} = \{u\}. \qquad (6b)$$

If a body force is applied in the layer, the total displacement and the stress fields can be written as:

$$\{u\}_T = \{u\}_F + \{u\} \qquad (7a)$$

$$\{\sigma\}_T = \{\sigma\}_F + \{\sigma\}. \qquad (7b)$$

Here, the subscript "F" denotes that the field is due to the same body force as applied in the "full" space case, and "T" denotes that the field is contributed from both the body forces and the boundary conditions. By substituting equations (7a) and (7b) into equation (6b), one obtains the result:

$$[f_v]\{\sigma\}_T = \{u\}_T + [f_v]\{\sigma\}_F - \{u\}_F. \qquad (8)$$

Next, the displacement and stress fields, $\{u\}_F$ and $\{\sigma\}_F$, due to a unit vertical point force applied at x_o will be constructed. In this case, the displacement field in the spatial domain is

$$u_{zF} = C[\kappa/R + (z-z_o)^2/R^3] \qquad (9a)$$

$$u_{rF} = Cr(z-z_o)/R^3. \qquad (9b)$$

Here,

$$C = 1/16\pi\mu(1-\nu), \quad R = |x-x_o|, \quad r = [R^2-(z-z_o)^2]^{1/2}. \qquad (9c)$$

The displacement and stress fields in the transformed domain are obtained by performing the related Hankel transforms as given in equations (2a)-(2b). The results are:

$$U_{zzF} = C[\kappa/\xi + |z-z_o|]\exp(-\xi|z-z_o|) \qquad (10a)$$

$$U_{rF} = C(z-z_o) \quad \exp(-\xi|z-z_o|) \qquad (10b)$$

$$S_{zzF} = -2\mu C[(2-2\nu)\text{sgn}(z-z_o)$$

$$+ \xi(z-z_o)]\exp(-\xi|z-z_o|) \qquad (11a)$$

$$S_{rzF} = -2\mu C[1-2\nu+\xi|z-z_o|] \quad \exp(-\xi|z-z_o|). \qquad (11b)$$

Then $\{\sigma\}_F$ and $\{u\}_F$ in equation (8) are obtained by substituting $z = 0$ and $z = H$ into equations (10a)-(11b) in the forms of equations (4a)-(4b).

If the layer is replaced by an upper half space, then $A_3 = A_4 = 0$ in equation (3), and there is no change in the formulation. Hence, the half space solution may be viewed as a special case of a layer solution.

For a multilayered system that contains N layers, the remaining procedure is to assemble the matrix of each single layer to form the global matrix. To demonstrate the assembly process, two consecutive layers i and $i+1$ are considered. If layer i is above layer $i+1$, the interfacial conditions are:

$$\{S_{zz}(0_i), S_{rz}(0_i)\}_T = \{S_{zz}(H_{i+1}), S_{rz}(H_{i+1})\}_T \qquad (12a)$$

$$\{U_{zz}(0_i), U_r(0_i)\}_T = \{U_{zz}(H_{i+1}), U_r(H_{i+1})\}_T. \qquad (12b)$$

The flexibility matrix after assembling is:

$$[\mathbf{F}_v] = [\mathbf{f}_v]_i + [\mathbf{f}_v]_{i+1}.$$

The transposed vector of $\{\sigma\}_T$ is:

$$\{S_{zz}(H_i), S_{rz}(H_i), S_{zz}(0_i), S_{rz}(0_i), S_{zz}(0_{i+1}), S_{rz}(0_{i+1})\}_T.$$

The transposed vector of $\{u\}_T$ is:

$$\{-U_{zz}(H_i), -U_r(H_i), 0., 0., U_{zz}(0_{i+1}), U_r(0_{i+1})\}_T.$$

The forcing terms are:

$$([\mathbf{f}_v]\{\sigma\}_F - \{u\}_F)_i + ([\mathbf{f}_v]\{\sigma\}_F - \{u\}_F)_{i+1}.$$

(B) Asymmetric Case. After discussing the process to solve the axially symmetric case, the displacement and the stress fields due to a point "horizontal" force are considered. Similarly to equation (8), the layer equation is:

$$[\mathbf{f}_h]\{\sigma_h\}_T = \{u_h\}_T + [\mathbf{f}_h]\{\sigma_h\}_F - \{u_h\}_F \qquad (13)$$

Here, the goal is to construct the matrix $[\mathbf{f}_h]$, and vectors $\{\sigma_h\}_F$ and $\{u_h\}_F$ in equation (13). It should be kept in mind that $[\mathbf{f}_h]$ depends on the definition of $\{u_h\}$ and $\{\sigma_h\}$.

It is well known that the displacement field due to a unit horizontal point force applied at $\mathbf{x}_o$ in the full space is:

$$u_{zF} = Cr(z - z_o)\cos\theta/R^3 \qquad (14a)$$

$$u_{rF} = C[\kappa/R + r^2/R^3]\cos\theta \qquad (14b)$$

$$u_{\theta F} = -C\kappa\sin\theta/R \qquad (14c)$$

where $r\cos\theta = x - x_o$, $r\sin\theta = y - y_o$. Thus, the angular dependence for the potentials in equations (1) are

$$(\phi_z, \phi_r, \phi_\theta) = (\Phi_z\cos\theta, \Phi_r\cos\theta, \Phi_\theta\sin\theta),$$

which are solved by the first order Hankel transform; the results are:

$$\Phi_j = \int_0^\infty \{B_j\exp(-\xi z) + B_{j+3}\exp[\xi(z - H)]\}\xi J_1(\xi r)d\xi \qquad (15)$$

where $(\Phi_1, \Phi_2, \Phi_3) = (\Phi_z, \Phi_r, \Phi_\theta)$. By substituting equation (15) into equations (1), the displacements field in terms of B_j is obtained. The stress field is obtained by differentiating the displacement field. The results are in the following compact forms:

$$\{u_z/c, u_r/c + u_\theta/s, u_r/c - u_\theta/s,$$

$$\sigma_{zz}/c, \sigma_{rz}/c + \sigma_{\theta z}/s, \sigma_{rz}/c - \sigma_{\theta z}/s\}$$

$$= \int_0^\infty \{U_z J_1(\xi r), U_p J_2(\xi r), U_m J_0(\xi r),$$

$$S_z J_1(\xi r), S_p J_2(\xi r), S_m J_0(\xi r)\}\xi d\xi \qquad (16)$$

where $c = \cos\theta$, $s = \sin\theta$ and

To obtain the flexibility matrix, $\{u_h\}$, $\{\sigma_h\}$ and $\{\mathbf{B}_h\}$ are defined as:

$$\{u_h\}^T = \{-U_z(H), -U_p(H),$$

$$-U_m(H), U_z(0), U_p(0), U_m(0)\} \qquad (18a)$$

$$\{\sigma_h\}^T = \{S_z(H), S_p(H), S_m(H), S_z(0), S_p(0), S_m(0)\}$$

$$(18b)$$

$$\{\mathbf{B}_h\}^T = \{B_1, B_2, B_3, B_4, B_5, B_6\}. \qquad (18c)$$

Then, the $\{u_h\} - \{\mathbf{B}_h\}$ and $\{\sigma_h\} - \{\mathbf{B}_h\}$ relationships are obtained by substituting $z = 0$ and $z = H$ into equations (17). The results are written as:

$$\{u_h\} = [\mathbf{f}_3]\{\mathbf{B}_h\} \qquad (19a)$$

$$\{\sigma_h\} = [\mathbf{f}_4]\{\mathbf{B}_h\} \qquad (19b)$$

where the flexibility matrix is

$$[\mathbf{f}_h] = [\mathbf{f}_3][\mathbf{f}_4]^{-1}. \qquad (20)$$

To obtain $\{u_h\}_F$ and $\{\sigma_h\}_F$, the appropriate Hankel transforms as indicated in equation (16) are performed on equation (14). The results are:

$$U_{zF} = C \quad (z - z_o) \quad \exp(-\xi|z - z_o|)$$

$$U_{pF} = C(1/\xi + |z - z_o|) \quad \exp(-\xi|z - z_o|)$$

$$U_{mF} = C[(7 - 8\nu)/\xi - |z - z_o|] \exp(-\xi|z - z_o|) \qquad (21)$$

$$S_{zF}/2\mu = C(1 - 2\nu - \xi|z - z_o|) \quad \exp(-\xi|z - z_o|)$$

$$S_{pF}/2\mu = C[-\xi(z - z_o)] \quad \exp(-\xi|z - z_o|)$$

$$S_{mF}/2\mu = C[(-4 + 4\nu)\text{sgn}(z - z_o) + \xi(z - z_o)]\exp(-\xi|z - z_o|).$$

Then, $\{u_h\}_F$ and $\{\sigma_h\}_F$ in equation (13) are obtained by substituting $z = 0$ and $z = H$ into equation (21) in the forms of equations (18a)-(18c).

Generally speaking, when the loading or boundary conditions are more complex, more terms for the Fourier series expansion may be needed. However, the formulation is basically the same as the first term expansion, and the main differences between the mth term and the first term are in the replacement of $J_0(\xi r)$, $J_1(\xi r)$, $J_2(\xi r)$ by $J_{m-1}(\xi r)$, $J_m(\xi r)$, $J_{m+1}(\xi r)$.

3 Integral Equation and Numerical Scheme

To set up the integral equation, two symbols, $G_{ik}(\mathbf{x}, \mathbf{x}_o)$ and $\tau_{ijk}(\mathbf{x}, \mathbf{x}_o)$, are introduced, where $G_{ik}(\mathbf{x}, \mathbf{x}_o)$ is a representation for the ith direction displacement at x due to a unit point force applied along kth direction at $\mathbf{x}_o$ and $\tau_{ijk}(\mathbf{x}, \mathbf{x}_o)$ is the corresponding ij stress component. The processes required to derived the Green's functions have been described in Section 2. For a vertical planar crack with surface normal to x axis, the

$$\left\{\begin{array}{c} U_z \\ U_p \\ U_m \\ S_z/2\mu\xi \\ S_p/2\mu\xi \\ S_m/2\mu\xi \end{array}\right\} = \left[\begin{array}{cccccc} -1 & -\kappa - \xi z & 0 & 1 & -\kappa + \xi z & 0 \\ -1 & -\xi z & 2 & -1 & -\xi z & 2 \\ 1 & \xi z & 2 & 1 & \xi z & 2 \\ 1 & 2 - 2\nu + \xi z & 0 & 1 & -2 + 2\nu + \xi z & 0 \\ 1 & 1 - 2\nu + \xi z & -1 & -1 & 1 - 2\nu - \xi z & 1 \\ -1 & -1 + 2\nu - \xi z & -1 & 1 & -1 + 2\nu + \xi z & 1 \end{array}\right] \left\{\begin{array}{c} B_1\xi\exp(-\xi z) \\ B_2\exp(-\xi z) \\ B_3\xi\exp(-\xi z) \\ B_4\xi\exp[\xi(H - z)] \\ B_5\exp[\xi(H - z)] \\ B_6\xi\exp[\xi(H - z)] \end{array}\right\} \qquad (17)$$
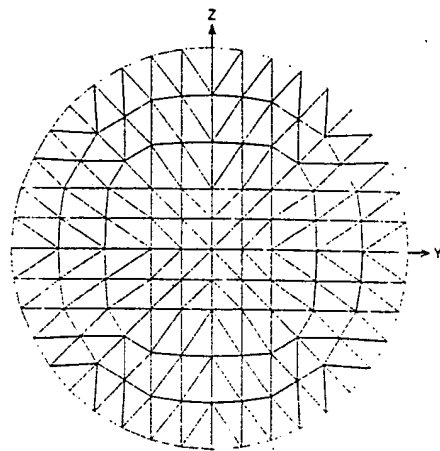
Fig. 1 The mesh and the coordinate system of the numerical examples

Fig. 3 The normalized crack opening, $\mu\Delta u_1/p(2ae)^{1/2}$, along the edge of the crack, angle $\gamma = \tan^{-1}(z/y)$ for bimaterials
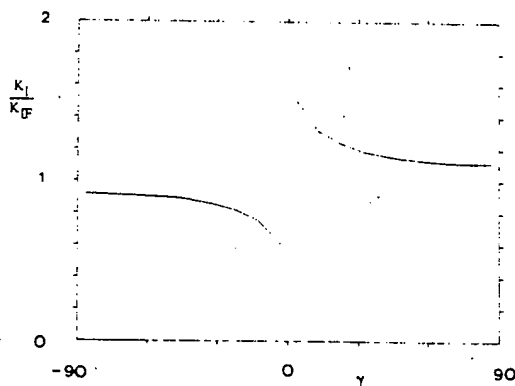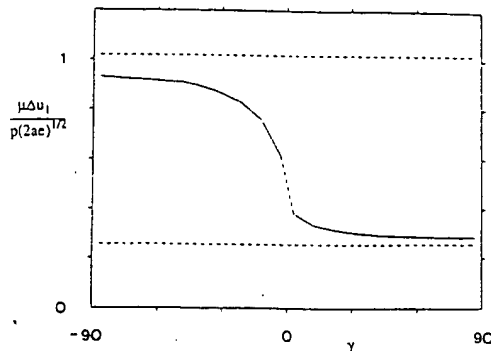

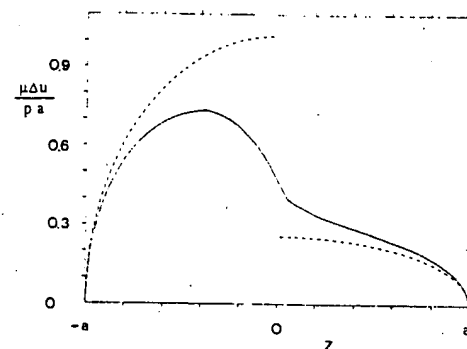
Fig. 2 The normalized stress intensity factor, K_I/K_{IF}, along the edge of the crack, angle $\gamma = \tan^{-1}(z/y)$ for bimaterials

Fig. 4 The normalized crack opening, $\mu\Delta u_1/pa$, along the Z-axis for bimaterials

integral representation for the displacement field due to the mode I crack opening displacement is:

$$u_k(\mathbf{x}_o) = \int \tau_{11k}(\mathbf{x}; \mathbf{x}_o)\,\Delta u_1(\mathbf{x})dA(\mathbf{x}). \qquad (22)$$

In Appendix B, it is shown that equation (22) can be derived from the equivalent body force method.

The integral equation is obtained by applying Hooke's law to equation (22) and applying the pressure boundary condition along the crack surface. The result is:

$$-p(\mathbf{x}_o) = \sigma_{11}(\mathbf{x}_o) = \int K(\mathbf{x}, \mathbf{x}_o)\Delta u_1(\mathbf{x})dA(\mathbf{x}) \qquad (23)$$

where

$$K(\mathbf{x}, \mathbf{x}_o) = 2\mu_o\{(1-\nu_o)\tau_{111,xo} + \nu_o[\tau_{112,yo} + \tau_{113,zo}]\}/(1-2\nu_o)$$

$$(24)$$

and $\mu_o = \mu(\mathbf{x}_o)$, $\nu_o = \nu(\mathbf{x}_o)$. Details concerning $K(\mathbf{x}, \mathbf{x}_o)$ are given in Appendix C. Numerically, equation (23) is written in discrete form as:

$$p(\mathbf{x}_o) = \int_o^\infty d\xi \left[\sum_{m=1}^M \int_{S_m} K(\mathbf{x}; \mathbf{x}_o;\xi)\Delta\dot{u}_1(\mathbf{x})w(\mathbf{x})dA(\mathbf{x}) \right] \qquad (25)$$

where $w(\mathbf{x})$ is the weighting function for the crack opening displacement, i.e., $\Delta u_1(\mathbf{x}) = w(\mathbf{x})\Delta u_1(\mathbf{x})$, $K(\mathbf{x}, \mathbf{x}_o; \xi)$ is the kernel in ξ domain, and S_m is the subdomain. The numerical integration over the S_m domain is described by Lin and Keer (1987).

4 Numerical Examples and Discussions

The mesh and the coordinate system of the numerical examples are shown in Fig. 1. The crack is a penny-shaped crack, radius a, and the materials consist of an upper half space, a central layer, and a lower half space. The central layer represents the pay zone, while the upper and the lower half spaces represent barriers. The exact properties of the materials and the locations of the two interfaces are specified in the examples. The loading is by a constant fluid pressure p, applied on the crack surfaces.

In the first example, two interfaces are located at $z = 0$ and $z = 0.3a$. The shear moduli of the upper half space, the central layer and the lower half space are 4μ, 4μ, and μ, respectively. The Poisson's ratios are 0.2 for all materials. For this case, the kernel K has a closed form (Lee and Keer (1986)) which can be used to check the numerical integrations of the Hankel transforms. After checking, the Hankel transforms are performed by Simpson's rule with 400 integration points and with the maximum $\xi = 160/a$. In Fig. 2, the normalized stress intensity factor along the crack edge is plotted. The normalized factor $K_{IF} = 2p(a/\pi)^{1/2}$ corresponds to the stress intensity factor for a penny-shaped crack in fully space subjected to uniform tension. The result is same as in a previous paper by Lin and Keer (1988). It is noted that the stress intensity factor is greater than K_{IF} in the upper medium and is smaller than K_{IF} in the lower medium. The stress intensity factor at or near the interface is arguable because the point singularity at the intersection is not taken into account by the weighting function. In Fig. 3, the crack opening is plotted along the edge. The curved line gives the crack opening divided by the weighting function, $(2ae)^{1/2}$, where e is the distance from the collocation point in the boundary element to the crack edge. To understand this curve, two extreme cases are compared. When the shear modulus in the region $z > 0$ is replaced by μ, then, from the full space solution, $\mu\Delta u_1/p(2ae)^{1/2} = 4(1-\nu)\pi$, which is an
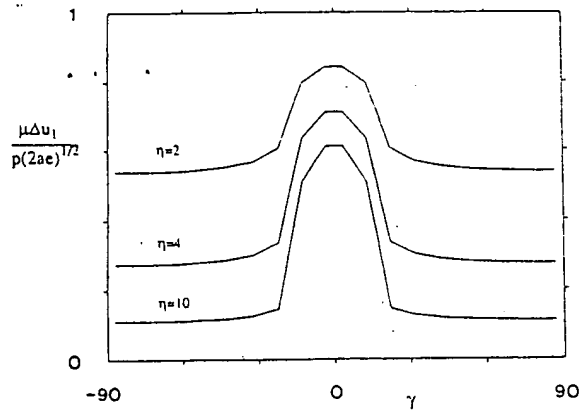
Fig. 5 The normalized crack opening, $\mu \Delta u_1/p\,(2ae)^{1/2}$, along the edge of the crack, angle $\gamma = \tan^{-1}\,(z/y)$ for trimaterials

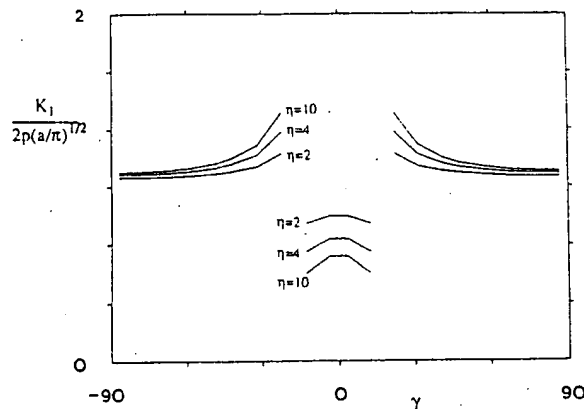Fig. 7 The normalized crack opening, $\mu \Delta u_1/pa$, along the Y-axis for trimaterials

Fig. 6 The normalized stress intensity factors $K_1/[2p(a/\pi)^{1/2}$ along the edge of the crack, angle $\gamma = \tan^{-1}\,(z/y)$ for trimaterials

Fig. 8 The normalized crack opening, $\mu \Delta u_1/pa$, along the Z-axis for trimaterials

upper bound for the crack opening (upper dashed line). When the shear modulus for $z < 0$ is replaced by 4μ, then, $\mu\Delta u_1/p\,(2ae)^{1/2} = (1 - \nu)/\pi$, which is a lower bound for the crack opening (lower dashed line). The crack opening along the edge is decreasing from the lower medium to the upper medium because the upper medium is stiffer. Rapid changes occur near the interface. In Fig. 4, the crack opening along $y = 0$ is plotted. The two dashed lines correspond to the upper bound, $\mu\Delta u_1/pa = 4(1 - \nu)[1^2 - (z/a)^2]^{1/2}/\pi$, and the lower bound, $\mu\Delta u_1/pa = (1 - \nu)[1^2 - (z/a)^2]^{1/2}/\pi$, of the crack opening as in the previous discussion.

In the second example, two interfaces are located at $z = 0.3a$ and $z = -0.3a$. The shear modulus is μ for the central layer and $\eta\mu$ for the upper and lower half spaces. The Poisson's ratio is 0.2 for all materials. The three curves shown in Fig. 5 are the opening around the edge divided by the weighting function for $\eta = 2, 4$, and 10. The lower bound for these curves are $\mu\Delta u_1/p\,(2ae)^{1/2} = 4(1 - \nu)/\eta\pi = 1.02/\eta$. The three curves in Fig. 6 are the corresponding stress intensity factors. The conclusions are the same as the those obtained in the previous example: the opening in the softer medium is larger, rapid changes in crack opening occur around interfaces, and the stiffer region has a higher stress intensity factor. Figures 7 and 8 are the corresponding crack opening along Y axis and Z axis, respectively.

Remarks: First, if there are many layers in the system, the method of propagator matrices given in Appendix A is recommended. The flexibility matrix is used here only because there are only two interfaces. Second, the current approach can be applied in the frequency domain (see Xu and Mal (1987)).
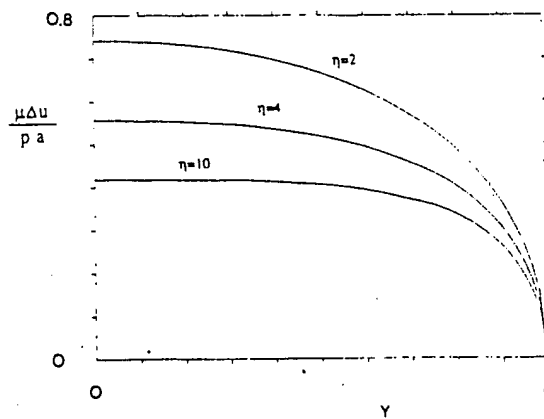
Even for the transversely isotropic medium, the current approach is also applicable (see Small (1986)).

5 Acknowledgment

References

Bazant, Z. P., and Estenssoro, L. F., 1979. "Surface Singularity and Crack Propagation," *International Journal of Solids and Structures*, Vol. 15, pp. 405–426 and Vol. 16, pp. 479–481.

Benthem, J. P., 1977, "State of Stress at the Vertex of a Quarter-Infinite Crack in a Half-Space," *International Journal of Solids and Structures*, Vol. 13, pp. 479–492.

Chan, K. S., Karasudhi, P., and Lee, S. L., 1974, "Force at a Point in the Interior of a Layered Elastic Half Space," *International Journal of Solids and Structures*, Vol. 10, pp. 1179–1199.

Fuchs, K., 1968, "The Reflection of Spherical Waves from Transition Zone with Arbitrary Depth-Dependent Elastic Moduli and Density," *Journal of Physics of the Earth*, Special Issue, Vol. 16, pp. 27–41.

Fuchs, K., and Muller, G., 1971, "Computation of Synthetic Seismograms with the Reflectivity Method and Comparison of Observations," *Geophysical Journal of the Royal Astronomical Society*, Vol. 23, pp. 417–433.

Gilbert, F., and Backus, G. E., 1966, "Propagator Matrices in Elastic Wave and Vibration Problems," *Geophysics*, Vol. 31, pp. 326–332.

Green, A. E., and Zerna, W., 1954, *Theoretical Elasticity*, Oxford Univ. Press, pp. 169–171.

Haskell, N. A., 1953, "The Dispersion of Surface Waves on a Multilayered Media," *Bulletin of the Seismological Society of America*, Vol. 43, pp. 17–34.

Krenk, S., and Schmidt, H., 1982, "Elastic Wave Scattering by a Circular Crack," *Philosophical Transactions of the Royal Society of London*, Ser. A308, pp. 167–192.

Kundu, T., and Mal, A. K., 1985, "Elastic Waves in a Multilayered Solid Due to a Dislocation Source," *Wave Motion*, Vol. 7, pp. 459-471.

Lee, J. C., and Keer, L. M., 1986, "Study of a Three-Dimensional Crack Terminating at an Interface," ASME JOURNAL OF APPLIED MECHANICS, Vol. 53, pp. 311-316.

Lin, W., and Keer, L. M., 1987, "Scattering by a Planar Three-Dimensional Crack," *Journal of the Acoustical Society of America*, Vol. 82, No. 4, pp. 1442-1558.

Lin, W., and Keer, L. M., 1986, "Scattering by a Horizontal Subsurface Penny-Shaped Crack," *Proceedings of the Royal Society of London*, Ser. A408, pp. 277-294.

Lin, W., and Keer, L. M., 1988, "Growth of a Hydraulically Pressurized Fracture," *Engineering Fracture Mechanics*, Vol. 29, No. 4, pp. 473-481.

Luco, J. E., and Apsel, R. J., 1983, "On The Green's Functions For a Layered Half-Space, Part I," *Bulletin of the Seismological Society of America*, Vol. 73, No. 4, pp. 909-929.

Martin, P. A., and Wickham, G. R., 1983, "Diffraction of Elastic Waves by a Penny-Shaped Crack: Analytical and Numerical Results," *Proceedings of the Royal Society of London*, Ser. A390, pp. 91-129.

Mura, T., 1982, *Micromechanics of Defects in Solids*, Martinus Nijhoff, pp. 104-109.

Murakami, Y., and Nemat-Nasser, S., 1983, "Growth and Stability of Interacting Surface Flaws of Arbitrary Shape," *Engineering Fracture Mechanics*, Vol. 17, pp. 193-210.

Pao, Y. H., and Gajewski, R. R., 1977, "The Generalized Ray Theory and Transient Responses of Layered Elastic Solids," *Physical Acoustics*, Vol. 13, Academic Press, New York, pp. 183-265.

Small, J. C., and Booker, J. R., 1986, "Finite Layer Analysis of Layered Elastic Materials Using a Flexibility Approach. Part 2-Circular and Rectangular Loadings," *International Journal for Numerical Methods in Engineering*, Vol. 23, pp. 959-978.

Somaratna, N., and Ting, T. C. T., 1986, "Three-Dimensional Stress Singularities in Anisotropic Materials and Composites," *International Journal of Engineering Science*, Vol. 24, pp. 1115-1134.

Thomson, W. T., 1950, "Transmission of Elastic Waves Through a Stratified Solid Medium," *Journal of Applied Physics*, Vol. 21, pp. 89-93.

Weaver, J., 1977, "Three Dimensional Crack Analysis," *International Journal of Solids and Structures*, Vol. 13, pp. 321-330.

Xu, P. C., and Mal, A. K., 1987, "Calculation of the Inplane Green's Functions for a Layered Viscoelastic Solid," *Bulletin of the Seismological Society of America*, Vol. 77, No. 5, pp. 1823-1837.

APPENDIX A

Stiffness Matrix and Propagator Matrix

A1 Stiffness Matrix: To obtain the layer stiffness matrix, $\{u\}$ and $\{\sigma\}$ are defined as:

$$\{u\}^T = \{U_{zz}(H), U_r(H), U_{zz}(0), U_r(0)\} \quad (A1a)$$

$$\{\sigma\}^T = \{-S_{zz}(H), -S_{rz}(H), S_{zz}(0), S_{rz}(0)\}. \quad (A1b)$$

Then the $\{u\}-\{A\}$ and $\{\sigma\}-\{A\}$ relationships are obtained by substituting $z=0$ and $z=H$ into equations (3). The results are written in the same forms as equations (5a) and (5b); the stiffness matrix is:

$$[s_v] = [f_2][f_1]^{-1}. \quad (A2)$$

If a body force is considered, the equation for the layer is:

$$[s_v]\{u\}_T = \{\sigma\}_T + [s_v]\{u\}_F - \{\sigma\}_F. \quad (A3)$$

Where $\{u\}_F$ and $\{\sigma\}_F$ can be obtained from equations (10a)-(11b) and (A1a)-(A1b) by substituting $z=0$ and $z=H$.

For the case of applying a horizontal point force, the $\{u_h\}$ and $\{\sigma_h\}$ are defined as:

$$\{u_h\}^T = \{U_z(H), U_p(H), U_m(H), U_z(0), U_p(0), U_m(0)\}$$
$$(A4a)$$

$$\{\sigma_h\}^T = \{-S_z(H), -S_p(H), -S_m(H), S_z(0), S_p(0), S_m(0)\}$$
$$(A4b)$$

Then, the corresponding $[s_h]$, $\{\sigma_h\}_F$ and $\{u_h\}_F$ can be found by applying equations (17), (21) and (A4a)-(A4b).

A2 Propagator Matrix: To form the propagator matrix,

two vectors $\{T\}$ and $\{B\}$ for the top and bottom surfaces of a layer are defined as follows:

$$\{T\}^T = \{U_{zz}(H), U_r(H), S_{zz}(H), S_{rz}(H)\} \quad (A5a)$$

$$\{B\}^T = \{U_{zz}(0), U_r(0), S_{zz}(0), S_{rz}(0)\}. \quad (A5b)$$

By substituting $z=0$ and $z=H$ into equation (3) to find the $\{T\}-\{A\}$ and $\{B\}-\{A\}$ relationship, the results are:

$$\{T\} = [g_1]\{A\} \quad (A6a)$$

$$\{B\} = [g_2]\{A\}. \quad (A6b)$$

The propagator matrix $[P]$ is the relationship between $\{T\}$ and $\{B\}$, thus,

$$[P]\{T\} = \{B\} \quad (A7a)$$

$$[P] = [g_2][g_1]^{-1}. \quad (A7b)$$

To demonstrate how the propagator matrix works, two consecutive layers, i and $i+1$ are considered. Then,

$$[P]_i\{T\}_i = \{B\}_i \quad (A8a)$$

$$[P]_{i+1}\{T\}_{i+1} = \{B\}_{i+1}. \quad (A8b)$$

These two equations may be considered into one equation by applying the interfacial continuity condition,

$$\{B\}_i = \{T\}_{i+1}. \quad (A9)$$

The result is

$$[P]_{i+1}[P]_i\{T\}_i = \{B\}_{i+1}. \quad (A10)$$

Thus, if the system contains n layers, the relation between the top and the bottom surfaces are constructed as:

$$[P(system)]\{T\}_1 = \{B\}_n. \quad (A11a)$$

$$[P(system)] = [P]_n[P]_{n-1} \cdots \cdots [P]_2[P]_1. \quad (A11b)$$

Now, applying boundary conditions on the top surface of the first layer and on the bottom surface of the last layer, the remaining unknowns in $\{T\}_1$ and $\{B\}_n$ can be solved. After $\{T\}_1$ is solved, the remaining $\{T\}_i$ are obtained by

$$\{T\}_i = \{B\}_{i-1} = [P]_{i-1}\{T\}_{i-1}.$$

In the above process, the $[P]$ matrix is the downward propagator matrix. Alternatively, the upward propagator matrix in a layer also can be found by defining:

$$\{P_u\}\{B\} = \{T\} \quad (A12a)$$

$$[P_u] = [g_1][g_2]^{-1}. \quad (A12b)$$

Then, the system upward propagation matrix is

$$[P_u \text{ system}]\{B\}_n = \{T\}_1 \quad (A13a)$$

$$[P_u \text{ system}] = [P_u]_1[P_u]_2 \cdots \cdots [P_u]_{n-1}[P_u]_n. \quad (A13b)$$

Now, consider the case that a body force is present in the jth layer, the equation for this layer is:

$$[P]_j\{T\}_{Tj} = \{B\}_{Tj} + [P]_j\{T\}_{Fj} - \{B\}_{Fj}. \quad (A14)$$

The vectors $\{T\}_{Fj}$ and $\{B\}_{Fj}$ are easily obtained from equations (10a)-(11b). Next, both the downward and upward propagator matrices are applied to construct the relationships between the top and bottom surfaces. The result is:

$$[P]_j[P]_{j-1} \cdots [P]_1\{T\}_1 = [P_u]_{j+1} \cdots [P_u]_n\{B\}_n$$
$$+ [P]_j\{T\}_{Fj} - \{B\}_{Fj}. \quad (A15)$$

For the asymmetric case, the upward and downward propagator matrix are formed in the same manner. $\{T\}$ and $\{B\}$ are defined as:

$$\{T\}^T = \{U_z(H), U_p(H), U_m(H), S_z(H), S_p(H), S_m(H)\}$$

$$(A16a)$$

$$\{B\}^T = \{U_z(0), U_p(0), U_m(0), S_z(0), S_p(0), S_m(0)\}$$

$$(A16b)$$

From equations (17), (21), ($A16a$–b), the propagator matrices can be obtained.

APPENDIX B

Derivation of Integral Representation From Equivalent Body Force Method

When there is unbalanced strain, ϵ_{mn}, on a system, the equivalent body force on this system is $-C_{pqmn}\epsilon_{mn,q}$, where C_{pqmn} are elastic constants. This strain ϵ_{mn} is also called eigenstrain by Mura (1982). Hence, the displacement field due to this body force is:

$$u_k(x_o) = -\int C_{pqmn}\epsilon_{mn,q}(x)G_{kp}(x_o,x)dV(x) \qquad (B1)$$

where $G_{kp}(x_o,x)$, (Section 3), is the displacement along the k direction at x_o due to a p direction unit force at x. Because $G_{kp}(x_o,x) = G_{pk}(x,x_o)$ due to Betti's reciprocal theorem and $C_{pqmn} = C_{mnpq}$ by the symmetry properties of the elastic constants, equation ($B1$) is written as:

$$u_k(x_o) = \int \epsilon_{mn,q}(x)C_{mnpq}G_{pk}(x,x_o)dV(x). \qquad (B2)$$

Integrating by parts, the result is:

$$u_k(x_o) = -\int \epsilon_{mn}(x)C_{mnpq}G_{pk,q}(x,x_o)dV(x)$$

$$= \int \epsilon_{mn}(x)\tau_{mnk}(x,x_o)dV(x). \qquad (B3)$$

The meaning of τ_{mnk} is also stated in Section 3. Finally, ϵ_{mn} is integrated along the normal of the crack surface to obtain the crack opening; the result is the integral representation in equation (22).

APPENDIX C

Kernel

To evaluate $K(x,x_o)$ in equation (24), first consider $\tau_{113,zo}$. Since $x = x_o = 0$,

$$\tau_{113} = \tau_{\theta\theta3} = 2\mu[(1-\nu)u_r/r + \nu(u_{r,r}+u_{z,z})]/(1-2\nu). \quad (C1)$$

Substituting u_r and u_z, equations ($2a$)–(3), the result is:

$$\tau_{\theta\theta3} = \int_0^\infty [2\mu\xi^2/(1-2\nu)]\{2\nu[A_2\exp(-\xi z)$$

$$+ A_4\exp(\xi z - \xi H)]J_o(\xi r) + L_3 J_1(\xi r)/\xi r\}d\xi \qquad (C2)$$

and

$$L_3 = [-A_1 + (1-\xi z)A_2]\exp(-\xi z)$$

$$+ [A_3 + (1+\xi z)A_4]\exp(\xi z - \xi H). \qquad (C3)$$

To evaluate $\tau_{\theta\theta3,zo}$, first evaluate $\{A\}_{,zo}$. This evaluation is achieved by differentiating $\{\sigma\}_F$ and $\{u\}_F$ with respect to z_o in advance, see equations (4), ($10a$)–($11b$).

The τ_{111} and τ_{112} terms are a bit more difficult. However, because the layers are horizontal and material is isotropic within each layer, $\tau_{111,xo} = -\tau_{111,x}$, $\tau_{112,yo} = -\tau_{112,y}$ and $\tau_{112}(0,y-y_o,z) = \tau_{221}(y-y_o,0,z)$. Next, τ_{111} and τ_{221} are expressed in terms of τ_{rr1}, $\tau_{r\theta1}$, $\tau_{\theta\theta1}$. Then, performing the proper differentiation as indicated by equations (16)–(17), the results are:

$$\tau_{112,yo} = \int_0^\infty 2\mu\xi^3\{-U_p[J_1(\xi r)/\xi r - 3J_2(\xi r)/(\xi r)^2]$$

$$+ E_z[-J_o(\xi r) + J_1(\xi r)/\xi r]\}d\xi \qquad (C4)$$

$$\tau_{111,xo} = \int_0^\infty 2\mu\xi^3\{-3U_pJ_2(\xi r)/(\xi r)^2 + [2B_3\exp(-\xi z)$$

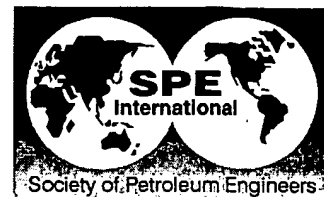$$+ 2B_6\exp(-\xi H + \xi z) - E_z]J_1(\xi r)/\xi r\}d\xi \qquad (C5)$$

where U_p is given in equation (17) and

$$E_z = 2\nu[B_2\exp(-\xi z) - B_5\exp(-\xi H + \xi z)]. \qquad (C6)$$

When x and x_o are in the same layer, the kernel $K(x,x_o)$ contains an extra term, the full space term, i.e.,

$$K_F(x,x_o) = \mu/4\pi(1-\nu)R^3. \qquad (C7)$$

GOHFER application (handwritten)

SPE 80935

Modeling of Hydraulic Fracture Height Containment in Laminated Sand and Shale Sequences

Jennifer L. Miskimins, SPE, Colorado School of Mines, and Robert D. Barree, SPE, Barree & Associates, Inc.

Abstract

The results of hydraulic fracture modeling in a hydrocarbon reservoir consisting of laminated sand and shale sequences are presented. Work previously published by other authors addresses hydraulic fracture growth characteristics in layered intervals, but little published information is available for growth in thin-bedded reservoirs. For the purposes of this paper, thin beds are considered to be on the order of less than 6 inches (15 cm) in thickness. In certain reservoirs, there may be thousands of these thin beds involved in influencing hydraulic fracture growth.

The hydraulic fracture modeling is based on data from the North LaBarge Shallow Unit (NLBSU) located in the Green River basin of Wyoming. The NLBSU produces hydrocarbons from the Cretaceous-age Mesaverde interval. This reservoir is comprised of laminated sand and shale sequences. Hydraulic fracturing is necessary for economic production. Actual field data from two NLBSU wells is used in the analysis. The data includes stimulation treatment pressures and information, as well as a radioactively tagged fracture treatment.

The hydraulic fracture modeling software GOHFER is used in the analysis. GOHFER is used based on its ability to approximate decoupled rock deformation with shear-slip, and its extensive use in the industry.

The results of this study strongly indicate that the sand and shale laminations present in the Mesaverde reservoir act as a hydraulic fracture height containment mechanism. Two events are presented as the reasons for this observed containment. First, shear slippage is prevalent due to the numerous interfaces present in the subject depositional environment. These interfaces inhibit fracture growth through shear failure. Second, the contrast in rock mechanical property values between the sand and shale intervals reduce the fracturing energy available for fracture propagation.

Further research in this area is strongly recommended due to the significant oil and gas reserves associated with this type of reservoirs. These additional research areas include laboratory investigations and field work with tiltmeter and microseismic analysis. Meanwhile, fracture modelers are strongly encouraged to evaluate the effects of laminations in their modeling efforts.

Introduction

Predicting hydraulic fracture growth patterns is the main goal of hydraulic fracture modeling. The modeling practitioner strives to create an input file that represents the nature of the reservoir as closely as possible. This paper describes modeling results from a depositional environment which requires a particularly detailed input model. The subject environment is laminated sand and shale sequences.

In 1977, Daneshy[1] provided one of the first investigations into hydraulic fracture growth in layered formations. He concluded that there was a significant relationship between the strength of the interface bond between two formations and whether or not a hydraulic fracture would cross the interface. Although Daneshy's work addressed layered formations, the results were limited to relatively thick layers of two or three rock types. He did conclude that slippage at the layer interfaces would be a relevant containment mechanism and that the thinner the layers, the better the chance for slippage to occur.

During the same time period as Daneshy's work, Simonson, et al, published results showing the significance of elastic properties, in-situ stresses, and pressure gradients on hydraulic fracture containment.[2] Since the work of Daneshy and Simonson, et al, several authors have published treatises addressing various containment mechanisms. In 1980, Hanson, et al, concluded that shear stress at an interface determines whether or not a fracture traverses the interface.[3] Warpinski, et al, showed that minimal in-situ stress contrasts could restrict fracture growth.[4] Warpinski and Teufel discussed how various geological features, such as joints, faults, and bedding planes, could affect hydraulic fracture growth.[5] More recently, in 1998, Barree and Winterfeld showed how interfacial slippage has a large influence on hydraulic fracture containment through shear decoupling.[6] Finally, in 2001, Smith, et al, discussed how modulus in layered situations can be incorrectly averaged, thus providing questionable results in modeling attempts.[7]

As discussed, References 1-7 provide a brief overview of the main mechanisms generally accepted as containment mechanisms in hydraulic fracture height growth. References 8-14 provide further considerations for hydraulic fracture height containment mechanisms and layered formation characteristics. However, there is little published information for hydraulic fracture growth in laminated rock formations. Although laminated formations are "layered," they are unique since there may be thousands of layers in a given zone of interest. These numerous layers are interactive and present unique problems in hydraulic fracture growth patterns.

This paper provides hydraulic fracture modeling results for a reservoir consisting of laminated sand and shale sequences. These sand and shale laminations range from 0.5 to 6 inches (1.3-15 cm) in thickness with an overall reservoir thickness of approximately 150 feet (46 m). Detailed model develop is discussed along with the modeling results. Conclusions based on the modeling results are presented.

Model Development
The North LaBarge Shallow Unit (NLBSU) is the field chosen for use in this study. The NLBSU is located in the Green River basin of Wyoming (**Figure 1**). The NLBSU produces oil and gas from the Cretaceous-age Mesaverde formation at an average depth of 2000 feet (610 m). A variety of research on the NLBSU geological setting and stratigraphy has been performed on the area during the last several years.[15-19] Hydraulic fracturing of the Mesaverde zone is necessary for economic production in the NLBSU.

Field Stratigraphy. The NLBSU Mesaverde formation consists of eight main subdivisions labeled C through H. A type log is shown in **Figure 2**. The Mesaverde produces from subdivisions F through H. **Figure 3** shows an eight inch (20 cm) section of core which displays the thin-bedded nature of the formation. These laminations are present throughout the entire Mesaverde interval and are broken down into distinctive sand and shale layers. **Figure 4** is an FMI log from NLBSU #9-16E that demonstrates the laminations seen in a 270-foot (82 m) interval of the Mesaverde. **Figure 5** is a 26-foot (8 m) section of this same log shown to further demonstrate the thin-bedded environment.

The thin beds and main subdivisions of the Mesaverde are the result of a series of transgressive and regressive deposits generated by eustatic sea-level changes, sediment influxes, and crustal movement during the Sevier Orogeny.[15,20]

Modeling Software. GOHFER (Grid-Oriented Hydraulic Fracture Extension Replicator) is the modeling software chosen for this project.[21] GOHFER is a 3D finite difference model. Reference 22 provides a comparison of GOHFER and other modeling software packages.

GOHFER was chosen for this project for a variety of reasons. First, the software is well known and used extensively in the petroleum industry for hydraulic fracture simulation. Second, GOHFER is a robust simulator and does not have a limit on the number of layers that can be incorporated in the input file. This was a critical consideration for the thin-bedded model used in this study.

Finally, GOHFER was selected for its ability to model decoupled rock deformations with shear-slip. Rocks rarely exhibit elastic behavior, but the equations used to drive most fracture simulators are based on the assumption of elastically coupled materials. Shear slippage is known to occur during fracturing operations based on the occurrence of microseismic activity.[23] In a sense, GOHFER can allow this slippage to occur. Since shear slippage is believed to be a significant containment mechanism,[1,6] the decoupling ability provides significant advantages in modeling the subject depositional environment.

In the GOHFER software, "process zone stress" controls allow the modeler to account for non-elastic behaviors, fluid lag, and tensile stress in the tip areas. A second input parameter, the "shear-decoupling radius" accounts for strain-energy losses at shear planes at a high angle relative to the direction of induced displacement (fracture width). The shear-decoupling reduces the full surface integral displacement solution so that only stresses acting over a local area affect the local displacement. This model drastically reduces the amount of strain energy concentrated at the tip of the fracture, removing the tip singularity and predicting improved containment.

Input Models. Two wells from the NLBSU, NLBSU #9-16E and NLBSU #64-16ED, are used in this study. Their selection is based on the extensive data set available for each well. Both wells were hydraulically fractured during completion and actual field data results are available. Additionally, the NLBSU #64-16ED treatment was radioactively tagged and logged before and after the treatment (three components of the fracture treatment were tagged including the pad fluid, the main 20/40 sand proppant, and the tail 16/30 sand proppant).

Three modeling cases are developed for each well. The first case for each well is a generic base case where detail is not stressed. These generic cases are labeled Case 1 and Case 2 for NLBSU #64-16ED and NLBSU #9-16E, respectively. Case 1 contains eight layers (4 sand and 4 shale), and Case 2 contains eleven layers (6 sand and 5 shale). A gamma ray cutoff of 60% shale established the breakdown of the sand and shale layers. These two cases mimic the failure to recognize the thin-bedded nature of the reservoir. The layers in Case 1 and 2 resemble the character of the type curve in Figure 2.

Cases 3 and 4 (NLBSU #64-16ED and NLBSU #9-16E, respectively) are developed as intermediate cases with more detail than Cases 1 and 2. The individual node size for Cases 3 and 4 are set with five-foot thicknesses, providing approximately 70 layers in the model. Extremely detailed rock mechanical property logs are available for these two wells from an earlier study,[17-18] and the GOHFER program read the rock property values (Young's Modulus, E, Poisson's Ratio, v) from a log data file based on a 1/10 inch resolution. The log data files are developed from the FMI log, thus providing the considerable resolution.

Cases 5 and 6 (NLBSU #64-16ED and NLBSU #9-16E, respectively) are developed in the same manner as Cases 3 and 4 with increased levels of detail (three-foot node thicknesses, providing approximately 120 layers in the model). All six cases are shown in **Table 1**.

With the varying degrees of detail established in the six cases, additional reservoir inputs such as permeabilities, leak-off coefficients, etc, are entered. The current fracturing procedure being used in the NLBSU provided the model inputs for fluid and proppant properties. The fluids consist of 25 lb linear and gelled water, and the proppants consist of 20/40 sand and 16/30 sand.

Modeling Results

The first step of the modeling procedure consisted of calibrating model results to the post-frac radioactive tracer log data from the NLBSU #64-16ED hydraulic fracture treatment. The authors recognize that results from tagged treatments have some limitations, especially if the fracture is not oriented along the wellbore axis, but the information provided by the post-treatment spectral gamma ray provides a starting point for calibration. **Figure 6** shows further reason for confidence in the information provided by the spectral gamma ray. Figure 6 shows the NLBSU #9-16E FMI log compared to the NLBSU #64-16ED post-treatment gamma ray. Although the depths of the wells are slightly different, there is a strong correlation between the major sand intervals of the FMI and the treatment placement indicated by the spectral gamma ray. Significant containment of the fracture treatment is suggested by the spectral gamma ray.

Using the pumping schedule, pressure information, and fracture height data from the actual NLBSU #64-16ED treatment, numerous model runs led to a modeling match for Case 1 for the critical data. However, this match could not be obtained without the addition of large process zone stresses in the highly laminated areas of the reservoir. The need for the large process zone stresses indicates significant tip effects are occurring during fracture growth. Additional runs led to similar modeling matches for Cases 2-6. During the modeling process, it was much easier to obtain data matches for the more detailed cases, Cases 5 and 6.

Modeling of the apparent fracture height containment could only be obtained with the addition of the process zone stresses to mimic tip effects. In order to compare what the models would look like if the modeler did not realize or suspect such containment, these stresses were eliminated and additional runs generated. **Table 2** shows the results of the models with and without process zone stresses.

Leakoff was incorporated in further runs for Cases 1-6 for sensitivity analysis. Minimal differences observed between the leakoff and non-leakoff cases are most likely due to the low permeability of the Mesaverde formation. Efficiencies around 50% occurred for all cases.

Discussion

Figures 7 and **8** show comparisons of predicted fracture height growth for Cases 1, 3, and 5 (NLBSU #64-16ED) and Cases 2, 4, and 6 (NLBSU #9-16E), respectively. **Figures 9** and **10** show comparisons of the model-predicted fracture half-length growth for Cases 1, 3, and 5 (NLBSU #64-16ED) and Cases 2, 4, and 6 (NLBSU #9-16E), respectively.

Figures 7 and 8 demonstrate the differences in height containment when significantly more detail is added to the model input. The fracture height growth in both wells is reduced by 25-40% between the general (Cases 1 and 2) and

the intermediate cases (Cases 3 and 4). The addition of layers to the intermediate cases had a distinct effect on the fracture growth pattern. Further addition of detail in Cases 5 and 6 provides an additional effect, but it is not as dramatic as the change between the first two types of circumstances. When compared to the information provided by the tracer log, the input models with more detail (Cases 3-6) appear to be more representative of what is actually happening in the reservoir. The height growth of 150-175 feet suggests the fractures are being contained in the gross reservoir sand intervals.

Figures 9 and 10 show the growth patterns of the model fracture half-lengths. As can be expected, the half-length growths tie closely with the height growths. For both Cases 1 and 2 the half-lengths reach a maximum point approximately 20 minutes into the treatment and then unrestricted height growth occurs.

The modeling performed during this study and actual field results strongly suggest that laminations present in the Mesaverde reservoir are affecting fracture growth patterns. The main influence appears to be in fracture height containment. Two mechanisms provide the most likely reasons for the observed containment. First, the thin-bedded nature of the Mesaverde provides numerous interfacial planes along which shear slippage can occur. As Daneshy[1] suggested, thinner rock layers increase the chance for slippage at the boundaries. Also, thinner layers lead to more discontinuities and increase chance of slip. Additionally, the Mesaverde is a naturally fractured formation, which provides additional areas for slippage to occur. Warpinski, et al, showed the Mesaverde formation is susceptible to shear slippage during pumping, as evidenced by microseismic events.[23]

The second suspected containment mechanism is the contrast in the rock mechanical properties of the sand and shale intervals. The Young's Modulus, E, values for the sand and shale in the subject reservoir differ by almost a factor of two. This has been confirmed with both core and sonic log measurements. Consider now that in general if a rock exhibits a high Young's Modulus, the net treating pressure will be greater and the width will be narrower than in a rock with a low Young's Modulus. Equations 1 and 2 demonstrate these concepts for a radial model:[24]

$$p_n \propto (E^{2n+1}K_n q^n)^{\frac{1}{(2n+2)}} (\frac{1}{r_f^{3n}})^{\frac{1}{(2n+2)}} \quad \dots \dots \dots (1)$$

$$w \propto (\frac{K_n q^n}{E})^{\frac{1}{(2n+2)}} (r_f^{2-n})^{\frac{1}{(2n+2)}} \quad \dots \dots \dots (2)$$

In these equations p_n is the net pressure, n is the power-law exponent for the fracturing fluid, K_n is the coefficient for the power-law fluid, r_f is the fracture radius, q is the flow rate in the fracture, and w is the average fracture width at the end of pumping.

As can be seen in Equation 1, as the Young's Modulus, E, value increases, the net pressure will increase. Conversely, in Equation 2, as the Young's Modulus increases, the width will decrease. For the NLBSU Mesaverde, as the fracture propagates across a thin bed with a low modulus, the net

pressure decreases and the width increases. Both of these factors; alone and in combination, cause energy to be lost and fracture growth to be hindered. This is not a new idea, but in a reservoir with hundreds, possibly thousands, of bed contrasts, the energy loss can be significant.

A related cause of shear-slip and bed decoupling is the stress concentration that develops at an interface between layers of different modulus. By Hooke's Law the deformation (strain) is directly related to the product of applied stress and modulus ($E\sigma$). If two dissimilar layers are coupled together and subjected to the same strain, caused by fracture width-opening, substantially different stresses will results in the two layers with a very high stress in the "stiff" layer and a lower stress in the "soft" material. The bonded interface between the layers becomes a focus of shear caused by the large differential stress across the boundary. In this case the shear slip or decoupling at the interface is caused by the induced deformation and does not occur except during fracture propagation. Once any slip occurs the tensile stress concentration at the tip of the fracture that allows the fracture to propagate as a "wedge" dissipates.

Fracture initiation across a shear-slip interface requires that local fluid pressure invade the rock layer across the shear plane, penetrate the rock, and overcome its current in-situ stress and intact rock strength. This is analogous to trying to split a board by applying fluid pressure to its flat surface. If the board surface is sealed against fluid penetration there is no lateral surface for the fluid pressure to act on and fracture initiation is difficult. If the board surface can be invaded by the fluid then the internal "pore" pressure can be easily increased and the wood can be split. The fundamental change from mechanical or "wedge" propagation to local pressure-parting is a potentially large part of the fracture containment mechanism at sheared interfaces.

Another contribution to shear stress development at a dissimilar material interface is the contribution of poro-elasticity through Biot's constant (α). In permeable sand the pore pressure is able to equilibrate during induced deformation. In impermeable shale the pore pressure is trapped and rises dramatically during deformation. This leads to a large drop in net normal force and helps to promote shear. This mechanism is again a result of induced deformation and does not show up as an identifiable stress or rock strength variation. Future work will focus on expanding the role of poroelasticity on fracture containment.

The combination of shear slippage and the corresponding loss of strain energy within a sequence of thin beds caused by rock mechanical property differences and induced stress variations suggest that significant height containment can be expected in the NLBSU Mesaverde interval. But these characteristics are not unique to this reservoir. Any formation that is comprised of laminations similar to the Mesaverde has the potential for significant containment that is not identifiable through routine stress profiling. The results of this study are not entirely conclusive for fracture growth in thin-bedded reservoirs, and the authors believe additional work should be performed in this area. Additional mapping techniques, such as tiltmeters and microseismic records, could help to confirm the suspected containment mechanisms. Additional laboratory testing would also be beneficial. In the meantime, operators should be aware of the potential growth restrictions in thin beds and design their hydraulic fracture treatments accordingly.

Conclusions

Hydraulic fracture growth in laminated sand and shale sequences has been examined using real data from the NLBSU Mesaverde reservoir and the hydraulic fracture modeling software GOHFER.

The conclusions from this study are as follow:

1. Hydraulic fracture modeling indicates laminated beds will affect fracture growth patterns. The effects are manifested in fracture height containment.
2. During modeling, significant process zone stresses had to be incorporated to mimic the non-elastic behavior of the Mesaverde formation. These process zone stresses account for non-elastic behaviors, fluid lag, and tensile stress in the fracture tip areas.
3. A combination of mechanisms appears to account for fracture height containment in the thin beds of the Mesaverde formation. These include shear slippage, rock mechanical property contrasts, poroelasticity (drained versus undrained deformation behavior), and fracture blunting. Each mechanism alone may affect fracture propagation, but the combined effect appears to be significant in laminated reservoirs.
4. Modelers should be aware of and account for the potential height containment caused by multiple layer discontinuities when designing fracture treatments for laminated reservoirs. If the potential containment is not accounted for, the entire reservoir interval may not be stimulated.
5. Additional work should be done to further the industry's knowledge of hydraulic fracture growth patterns in thin-bedded reservoirs. Significant reservoirs are produced from this type of depositional environment and further research would benefit reserve recoveries. This work may include laboratory analysis and fracture mapping techniques such as tiltmeters and microseismic surveys.

Acknowledgements

Nomenclature

E = Young's Modulus, psi
FMI = Formation Micro Imager
GOHFER = Grid-Oriented Hydraulic Fracture Extension Replicator
K_n = Coefficient for the power-law fluid
n = Power-law exponent for the fracturing fluid
p_n = Net pressure
q = Flow rate in the fracture
r_f = Fracture radius
w = Average fracture width, end of pumping
α = Biot's poroelastic constant
ν = Poisson's Ratio

References

1. Daneshy, A.A.: "Hydraulic Fracture Propagation in Layered Formations," SPE Paper No. 6088, SPE-AIME 51st Annual Fall Technical Conference and Exhibition, New Orleans, Louisiana (1977).
2. Simonson, E.R., Abou-Sayed, A.S., and Clifton, R.J.: "Containment of Massive Hydraulic Fractures," SPE Paper No. 6089, SPE-AIME 51st Annual Fall Technical Conference and Exhibition, New Orleans, Louisiana (1977).
3. Hanson, M.E., Anderson, G.D., and Shaffer, R.J.: "Effects of Various Parameters on Hydraulic Fracturing Geometry," SPE/DOE Paper No. 8942, SPE/DOE Symposium on Unconventional Gas Recovery, Pittsburg, Pennsylvania (1980).
4. Warpinski, N.R., Clark, J.A., Schmidt, R.A., and Huddle, C.W.: "Laboratory Investigation of the Effect of In-Situ Stresses on Hydraulic Fracture Containment," SPE Paper No. 9834, SPE Journal, (June 1982), p. 333-340.
5. Warpinski, N.R. and Teufel, L.W.: "Influence of Geologic Discontinuities on Hydraulic Fracture Propagation," SPE Paper No. 13224, Journal of Petroleum Technology, (February 1987), p. 209-220.
6. Barree, R.D. and Winterfeld, P.H.: "Effects of Shear Planes and Interfacial Slippage on Fracture Growth and Treating," SPE Paper No. 48926, SPE Annual Technical Conference and Exhibition, New Orleans, Louisiana (1998).
7. Smith, M.B., Bale, A.B., Britt, L.K., Klein, H.H., Siebrits, E., and Dang, X.: "Layered Modulus Effects on Fracture Propagation, Proppant Placement, and Fracture Modeling," SPE Paper No. 71654, SPE Annual Technical Conference and Exhibition, New Orleans, Louisiana (2001).
8. Fung, R.L, Vijayakumar, S., and Cormack, D.E.: "The Calculation of Vertical Fracture Containment in Layered Formations," SPE Paper No. 14707, SPE Formation Evaluation, (December 1987), p. 518-522.
9. Mendelsohn, D.A.: A review of hydraulic fracture modeling-II: 3D modeling and vertical growth in layered rock," J. of Energy Resources Tech., ASME, v. 106, p. 543-553.
10. Teufel, L.W. and Clark, R.A.: "Hydraulic Fracture Propagation in Layered Rock: Experimental Studies of Fracture Containment," SPE Journal, v. 24, no. 2, p. 19-32 (1984).
11. Usman, A.: "Fracture Height Prediction," SPE Paper No. 18338, Journal of Petroleum Technology, (July 1988), p. 813-815.
12. Van Eekelen, H.A.: "Hydraulic Fracture Geometry: Fracture Containment In Layered Formations," SPE Paper No. 9261, 55th Annual SPE Fall Technical Conference and Exhibition, Dallas, Texas (1980).
13. Wang, J.J. and Clifton, R.J.: "Numerical modeling of hydraulic fracturing in layered formations with multiple elastic moduli," Rock Mechanics Contributions and Challenges, Eds. Hustrulid and Johnson, Balkema, Rotterham, p. 303-310.
14. Warpinski, N.R., Schmidt, R.A., and Northrop, D.A.: "In-situ Stresses: The Predominant Influence on Hydraulic Fracture Containment," SPE Paper No. 8932, Journal of Petroleum Technology, (March 1982), p. 653-664.
15. Knight, C.N.: "Structural and Stratigraphic Controls on Mesaverde Reservoir Performance: North La Barge Field, Sublette County, Wyoming," Doctoral Thesis, Colorado School of Mines (1999).
16. Miskimins, J.L., Hurley, N.F., and Graves, R.M.: "3D Stress Characterization From Hydraulic Fracture and Borehole Breakout Data in a Faulted Anticline, Wyoming," SPE Paper No. 71341, SPE Annual Technical Conference and Exhibition, New Orleans, Louisiana (2001).
17. Miskimins, J.L: "The Effect of Thin-Bedded Sands and Shales on Hydraulic Fracture Growth Through the Use of Electrofacies and Hydraulic Fracture Modeling," Doctoral Thesis, Colorado School of Mines (2002).
18. Miskimins, J.L. Hurley, N.F., and Graves, R.M.: "A Method for Developing Rock Mechanical Property Logs Using Electrofacies and Core Data," SPE Paper No. 77783, SPE Annual Technical Conference and Exhibition, San Antonio, Texas (2002).
19. Miskimins, J.L., Graves, R.M., Hurley, N.F., and Barree, R.: "Extrapolation of Rock Mechanical Properties From a Cored Well to an Uncored Well Through the Use of Electrofacies," SPE/ISRM Paper No. 78250, SPE/ISRM Oil Rock 2002, Irving, Texas (2002).
20. Lawrence, D.T.: "Patterns and Dynamics of Late Cretaceous Marginal Marine Sedimentations: Overthrust Belt, Southwestern Wyoming," Doctoral Thesis, Yale University (1984).
21. Barree, R.D.: "A Practical Numerical Simulator for Three-Dimensional Fracture Propagation in Heterogeneous Media," SPE Paper No. 12273, Reservoir Simulation Symposium, San Francisco, California (1983).
22. Warpinski, N.R., Moschovidis, Z.A., Parker, C.D., and Abou-Sayed, I.S.: "Comparison Study of Hydraulic Fracturing Models: Test Case—GRI-Staged Field Experiment No. 3," SPE Paper No. 25890, SPE Rocky Mountain Regional/Low Permeability Reservoirs Symposium, Denver, Colorado (1993).
23. Warpinski, N.R., Branagan, P.T., Peterson, R.E., Wolhart, S.L., and Uhl, J.E.: "Mapping Hydraulic Fracture Growth and Geometry Using Microseismic Events Detected by a Wireline Retrievable Accelerometer Array," SPE Paper No. 40014, SPE Gas Technology Symposium, Calgary, Alberta, Canada (1998).
24. Gidley, J.L., Holditch, S.A., Nierode, D.E., and Veatch, R.W.J.: *Recent Advances in Hydraulic Fracturing*, Henry L. Doherty Series, v. 12, Richardson, Texas, SPE, 452 p. (1989).
25. Surdam, R.C.: "Natural Gas Resource Characterization Study of the Mesaverde Group in the Greater Green River Basin, Wyoming: A Strategic Plan for the Exploitation of Tight Gas Sands," GRI-93/0112, Laramie, Wyoming (1993).

SI Metric Conversion Factors

$$\text{in} \times 2.540\ \text{E}+00 = \text{cm}$$
$$\text{ft} \times 3.048\ \text{E}-01 = \text{m}$$
$$\text{psi} \times 6.894757 = \text{kPa}$$

TABLE 1: MODELING CASES			
Case Number	Well Name	Case Description	Number of Layers
1	NLBSU #64-16ED	General	8
2	NLBSU #9-16E	General	11
3	NLBSU #64-16ED	Intermediate	~70
4	NLBSU #9-16E	Intermediate	~70
5	NLBSU #64-16ED	Detailed	~120
6	NLBSU #9-16E	Detailed	~120

TABLE 2: MODELING RESULTS WITH AND WITHOUT PROCESS ZONE STRESSES		
Case Number	Fracture Half-Length-to-Height Ratio With Process Zone Stresses	Fracture Half-Length-to-Height Ratio Without Process Zone Stresses
1	2.23	0.54
2	4.48	0.61
3	5.03	0.64
4	1.75	0.59
5	3.34	0.61
6	2.85	0.62
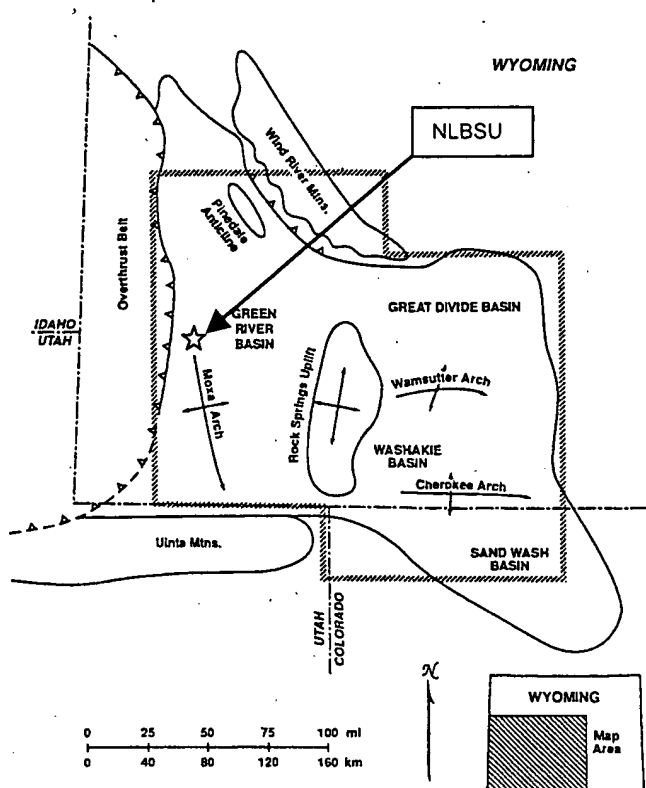
Figure 1: Green River basin location in Wyoming. The NLBSU is located at the northern extension of the Moxa Arch.[25]
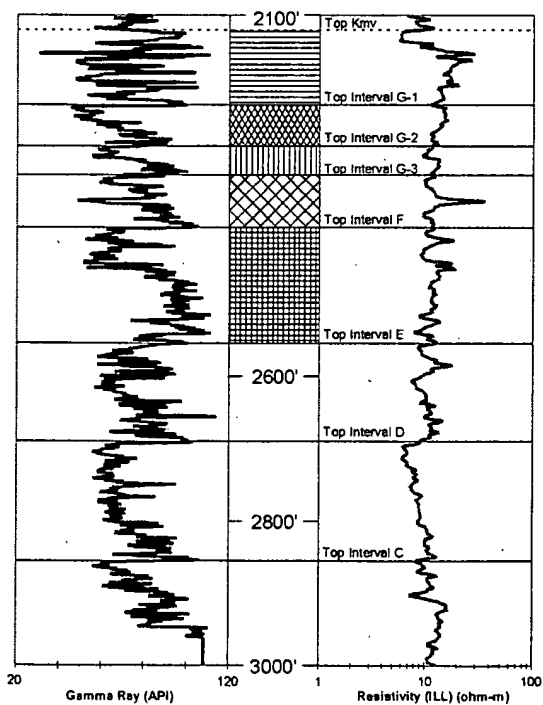
Figure 2: Type log from NLBSU #11-17E for the producing Mesaverde interval of North LaBarge field.[15]
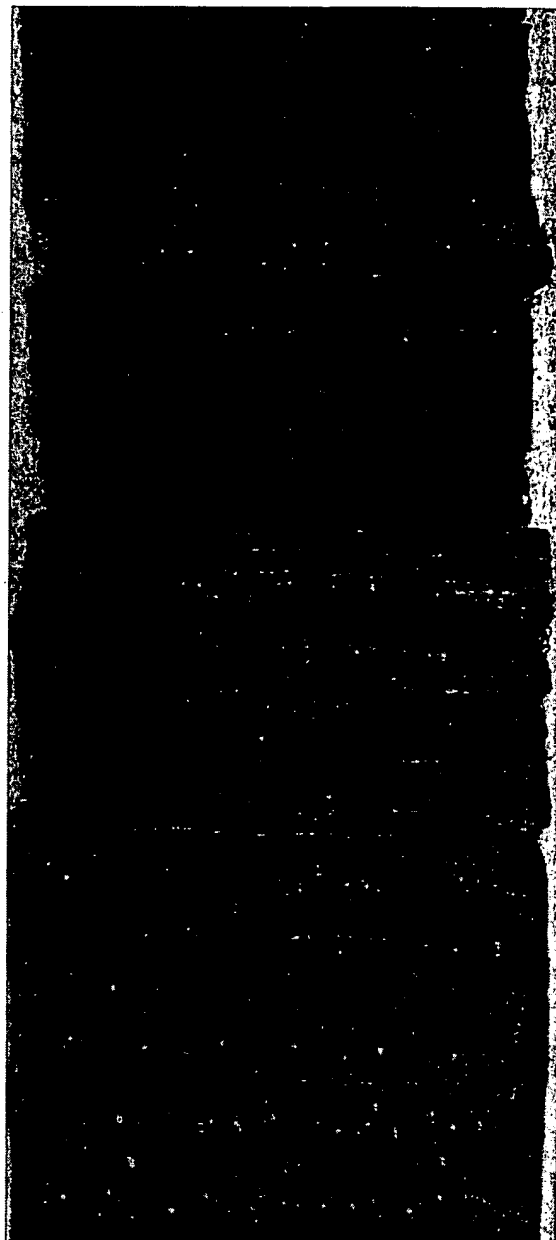
Figure 3: 8-inch core section from NLBSU #9-16E. Note the laminated, thin-bedded sand (light gray) and shale (dark gray) layers. The numbers represent inch measurements and the dots represent half-inch measurements.
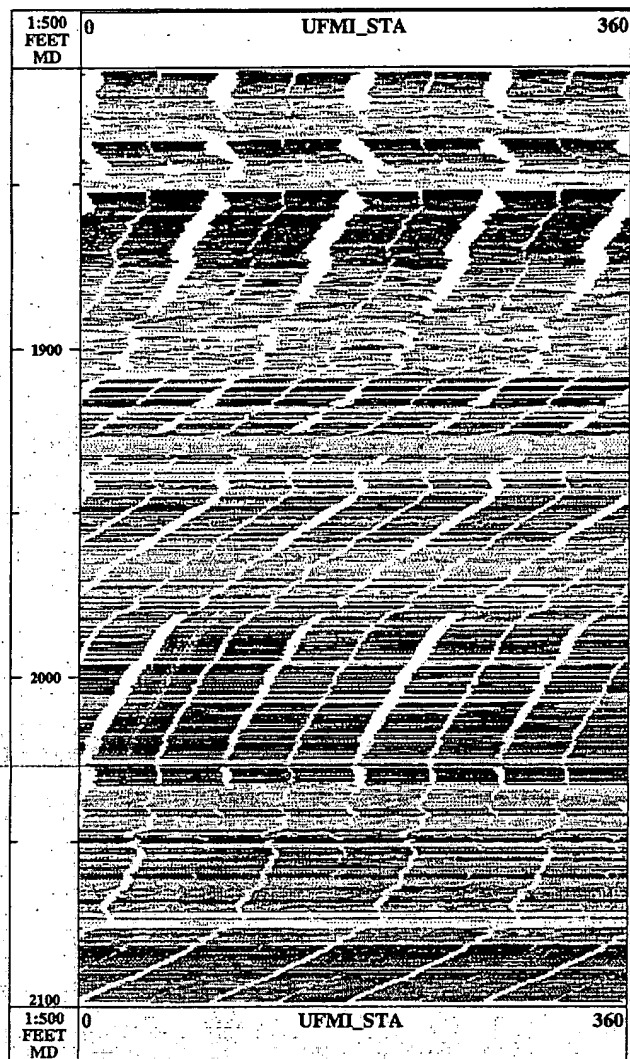
Figure 4: NLBSU #9-16E FMI log for the depths of 1815 to 2100 ft (584-640 m). Note the thin-bedded nature of the formation.
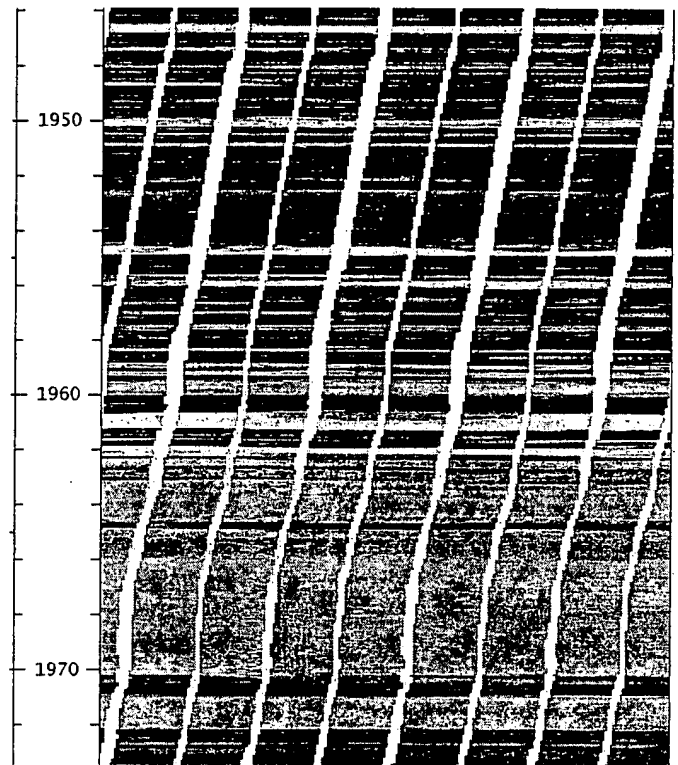
Figure 5: NLBSU #9-16E FMI log for the depths of 1946 to 1974 ft. Sand intervals are signified by the lighter yellow colors; shale intervals appear as the darker brown colors.
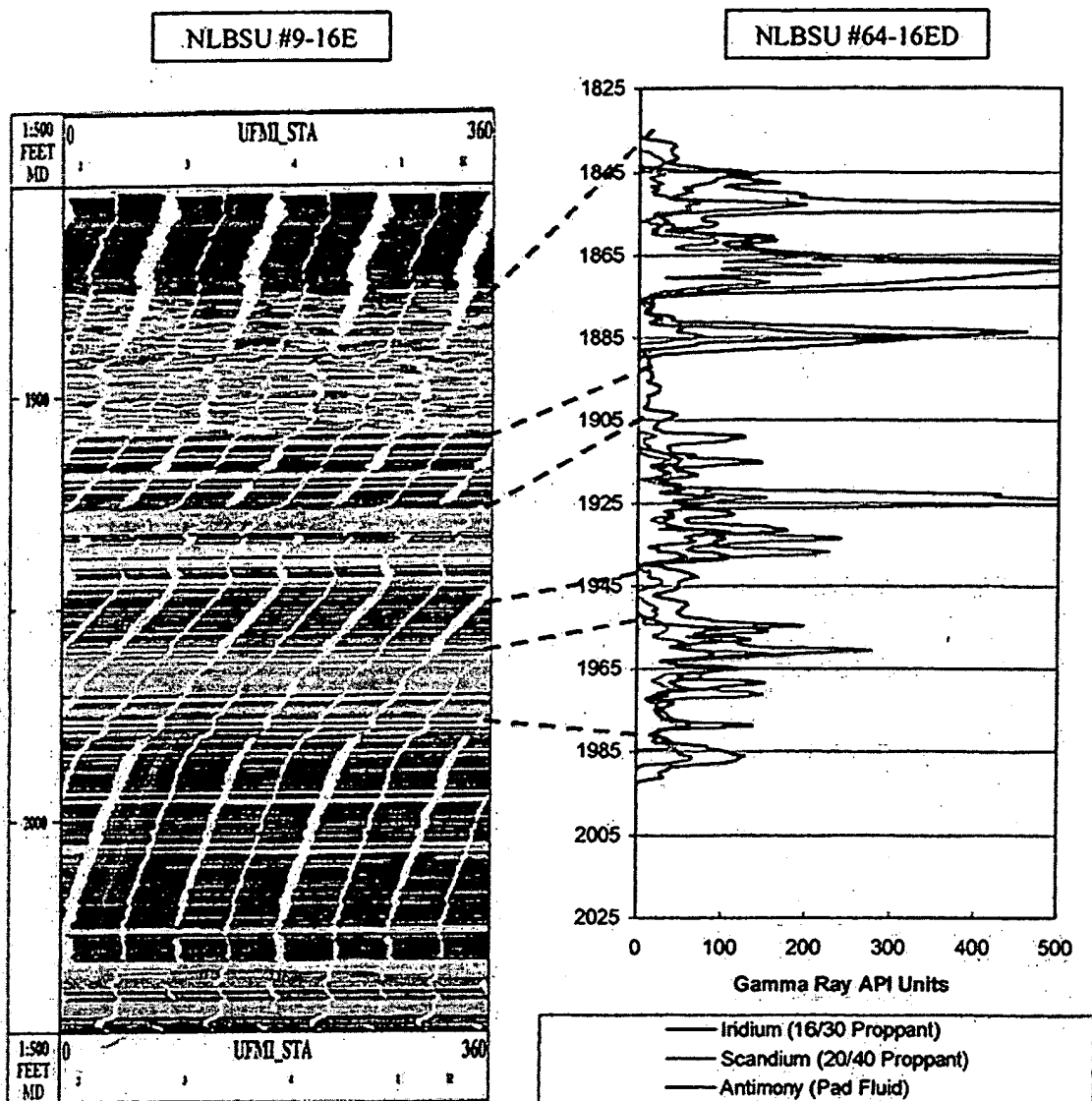
Figure 6: Comparison of the NLBSU #9-16E FMI image log and the NLBSU #64-16ED post-treatment gamma ray. Note the containment shown by the tracer for the major sand zones between 1840-1990 ft. Fracture height containment is suggested by the heavily laminated upper and lower shale zones.
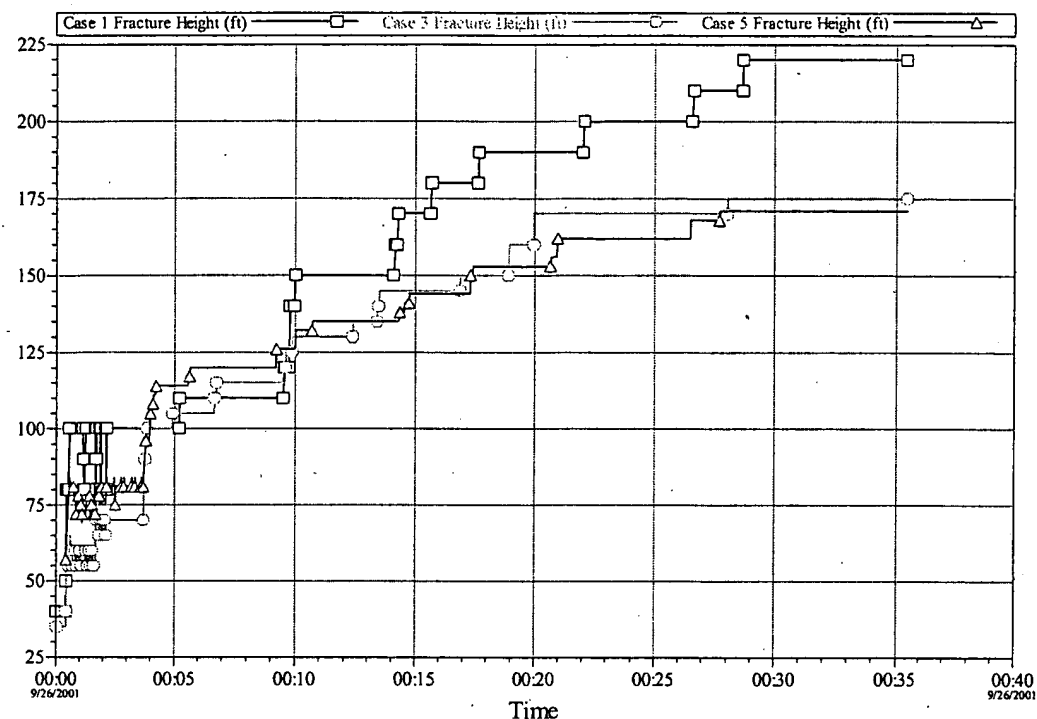
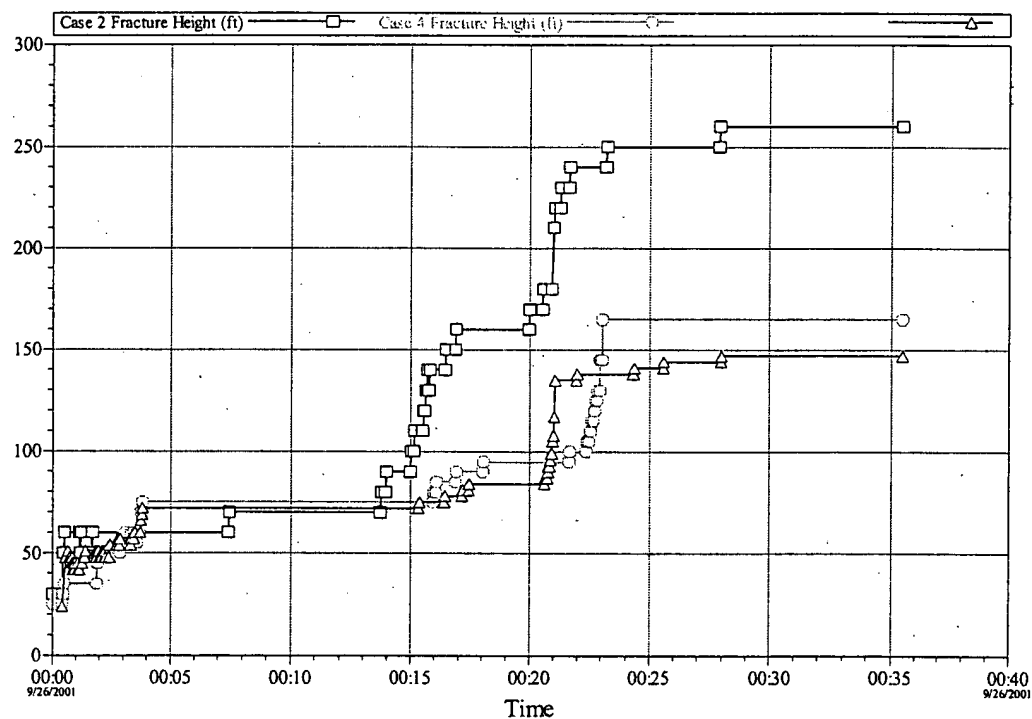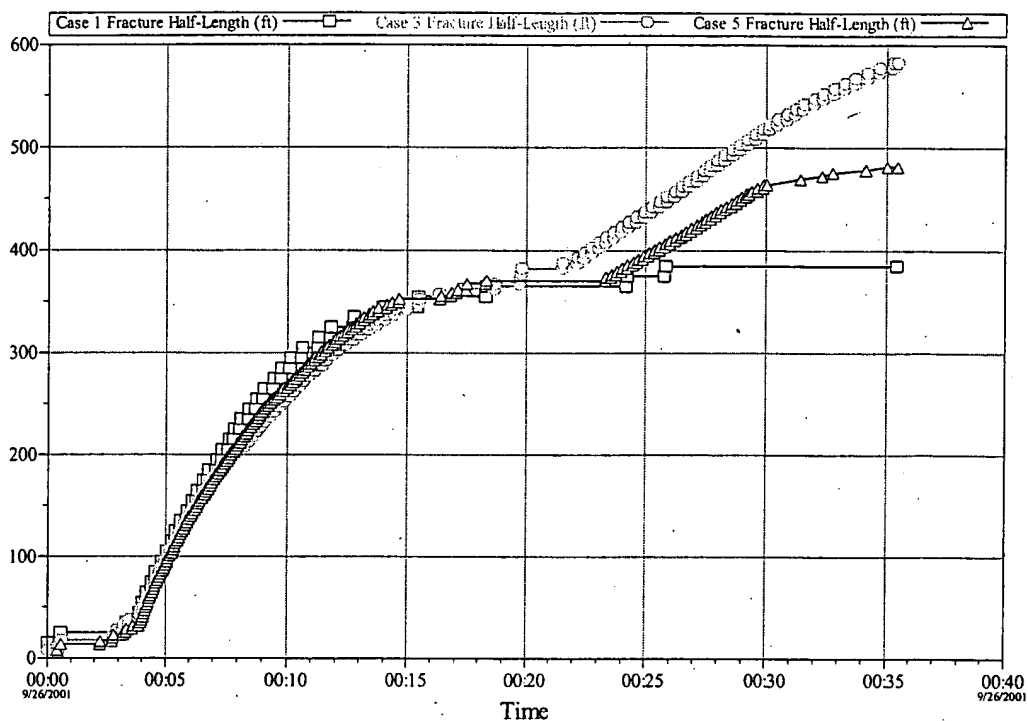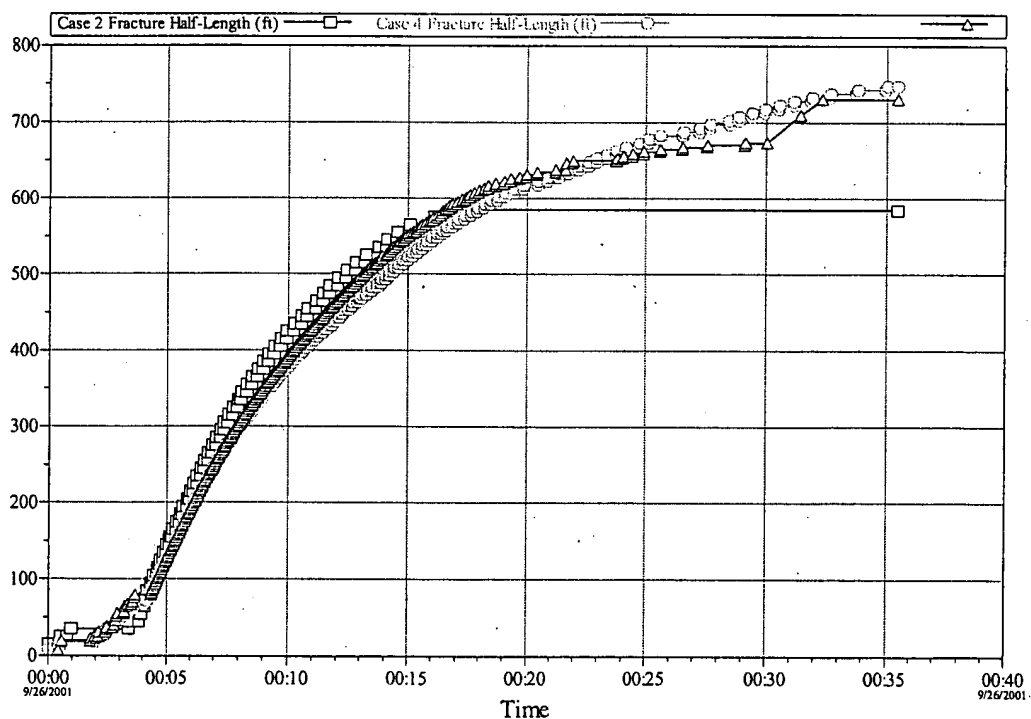Figure 7: Comparison of height growth patterns for Cases 1, 3, and 5 (NLBSU #64-16ED).

Figure 8: Comparison of height growth patterns for Cases 2, 4, and 6 (NLBSU #9-16E).

Figure 9: Comparison of fracture half-length growth patterns for Cases 1, 3, and 5 (NLBSU #64-16ED).

Figure 10: Comparison of fracture half-length growth patterns for Cases 2, 4, and 6 (NLBSU #9-16E).